Title
Numerical simulation of a closed rotor-stator system using Large Eddy Simulation

Author
Amouyal, Solal

Publication Date
2014

Peer reviewed|Thesis/dissertation

University of California
Los Angeles

Numerical simulation of a closed rotor-stator system using Large Eddy Simulation

A thesis submitted in partial satisfaction
of the requirements for the degree
Master of Science in Aerospace Engineering

by

Solal Abraham Teva Amouyal

2014

Abstract of the Thesis

Numerical simulation of a closed rotor-stator system using Large Eddy Simulation

by

Solal Abraham Teva Amouyal

Master of Science in Aerospace Engineering

University of California, Los Angeles, 2014

Professor Jeffrey D. Eldredge, Chair

A large eddy simulation of an enclosed annular rotor stator cavity is presented. The geometry is characterized by a large aspect ratio G = (b-a)/h = 18.32 and a small radius ratio a/b = 0.152, where a and b are the inner and outer radii of the rotating disk and h is the interdisk spacing. The rotation rate Ω under consideration is equivalent to the rotational Reynolds number $\mathrm{Re} = \Omega b^2/\nu = 9.5\text{x}10^4$, where ν is the kinematic viscosity.

The main objective of this study is to correctly simulate the rotor stator cavity using a low order numerical scheme on unstructured grids. The numerical simulations were run on the software AVBP developed by the *Centre Européen de Recherche et de Formation Avancée en Calcul Scientific*. The results were compared to the experimental results obtained by Sebastien Poncet of *Université Aix-Marseille*. Two large eddy simulations techniques were used: the Smagorinsky and Wall-adapting local eddy-viscosity models. The simulations were run on three set of grids, each with a different cell resolution-14, 35 and 50- along the thickness of the system. Results from each mesh show a good qualitative agreement of the mean velocity field with Poncet's experimental results. It was found that the Samgorinsky model is more appropriate for this configuration, due mainly to the associated strong turbulent viscosity which helps capture the large velocity gradients close to the disks.

The thesis of Solal Abraham Teva Amouyal is approved.

Ann Karagozian

John Kim

Jeffrey D. Eldredge, Committee Chair

University of California, Los Angeles

2014

Table of Contents

List of Figures

List of Tables

Acknowledgments

I want to thank the CERFACS for the great opportunity that was given to me. The short time spent there was very rewarding, both professionally and personally. Also in my thought are the nameless CERFACS doctorates and other staff members who never refused to come to the aid of the new intern. Special thanks go to Benedict Cuenot who accepted me in the program, Laurent Gicquel for supervising my work and of course Gabriel Staffelbach, for always being there when I needed help, and G-od knows I did!

I also want to acknowledge professors Ann Karagozian, John Kim and Jeff Eldredge for serving as members of my thesis committee.

CHAPTER 1

Introduction and Background

Fluid flows in rotor-stator systems are of great importance in scientific research and engineering practice. It is one of the most fundamental flow in fluid mechanics and has been studied for more than a century. It also has many engineering applications as the gas cooling of turbine blades or wind energy. Turbomachinery, which includes multiple rotor-stator stages, is responsible for more than 80% of the world's energy production today. Therefore, a good knowledge of heat transfer and fluid flows in rotor-stator systems is crucial. For example, an excessive amount of coolant is often supplied to the turbine cavity which imposes an unnecessary penalty on the engine cycle, which in turn induces a loss of efficiency.

In this study, the author focused on a simple, academic rotor-stator system. This configuration has been studied extensively experimentally, theoretically and numerically in literature and particularly by Sébastien Poncet of *Université Aix-Marseille*. Poncet's and Randriamampiania's experimental results [1] were chosen as a reference. Poncet has also studied the rotor-stator system numerically, using Reynolds Average Navier Stokes equations (RANS), Large Eddy Simulations (LES) and Direct numerical simulations (DNS). He often used high-order methods, such as probability density functions or the weighted essentially non-oscillatory schemes (WENO), with an axisymmetric structured grid build specifically for this geometry. The goal of this study is to reproduce S. Poncet's experimental results using low-order methods on an unstructured mesh. The software used is AVBP build by the *Centre Européen de Recherche et de Formation Avancée en Calcul Scientific* (CERFACS). Here, only LES is used.

First, the following section will summarise the research done on the rotor-stator cavity

in the 20^{th} century in a chronological fashion. Chapter 2 presents a throughout literature review of Poncet's work on rotor-stator systems with no through-flow. Then, in chapter 3, the governing equations and general methodology used in AVBP is presented followed by a review of the fundamentals of LES and the models used in the study. Chapter 4 then presents the numerical parameters and the meshes used followed by the simulation results; the last section of the chapter discusses the satisfaction and issues related to those results. Furthermore, the conclusion outlines the main findings of this study and the perspectives of further investigations.

1.1 Historical Context

The rotor-stator flow has been a fundamental problem for more than a century. It is one of the simplest flow where rotation plays a crucial role in turbulence. It also has an exact solution to the Navier-Stokes equations as found by Von Kármán [1].

The first work on this kind of flow is credited to Ekman. In 1905, he studied the effect of the rotating earth, approximated as a infinite plate, on the oceanic current [2]. Later, as previously mentioned, Von Kármán solved the Navier-Stokes equations for the laminar flow over an infinite rotating disk in a quiescent fluid [1]. He found that the flow is confined within a thin boundary layer on the rotating disk. Von Kármán analysis was subsequently followed by the work of Bödewadt. He studied the opposite case, in which an infinite stationary disk is sitting in a fluid in solid body rotation [3]. Batchelor studied the case of a fluid confined between two infinite disk, one rotating and one stationary [4]. He found the formation of a non-viscous core in solid body rotating confined between the boundary layer of each disk. However, Stewartson found in 1953 that the tangential velocity of the fluid is zero everywhere except in the rotor's boundary layer [5].

An intense controversy persisted for nearly thirty years after Stewartson's work. The problem of the existence or not of a core solid body rotation justified many works during that span of time. In 1983, Kreiss and Parter gave reason to both party proving the existence of a

multiple class of solutions, depending on the rotating speed of the rotor and the geometrical configuration of the system [6]. Daily and Nece performed theoretical and experimental studies on the closed rotor-stator system [7]. They pointed out that the different solutions were dependent on two non-dimensional numbers, the Reynolds number Re_Ω and the aspect ratio G:

$$Re_\Omega = \frac{\Omega b^2}{\nu} \qquad\qquad G = \frac{h}{b-a} \tag{1.1}$$

where Ω is the rotational velocity of the disk, a and b the inner and outer radius of the cavity respectively, and h the interspace between the two disks. Note that the Reynolds number is strictly a geometrical and fluid parameter, as it contains no information of the flow itself. The geometrical configuration of the system is shown in figure 1.1 [7].

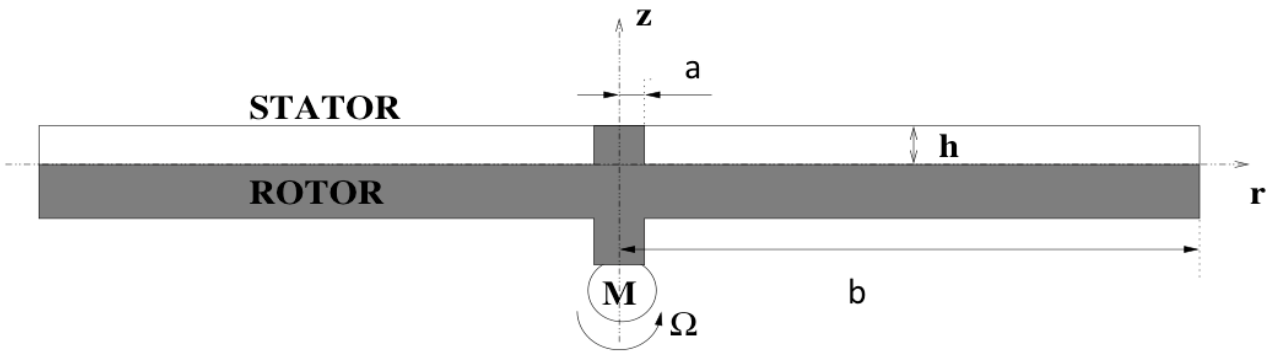

Figure 1.1: System geometry

Daily and Nece found the existence of four different regimes depending on the combination of the Reynolds number and aspect ratio: two laminar and two turbulent regimes, each of which corresponding either to merged or separated boundary layers. Their results are presented in figure 1.2.

Wether the flow is laminar or turbulent mostly depends on the Reynolds number. At $Re_\Omega \geq 2\text{x}10^5$, the flow will most likely be turbulent whatever the aspect ratio. The results of Daily and Nece were later confirmed numerically by that of Lance and Rogers [8], and Owen and Rogers [9].

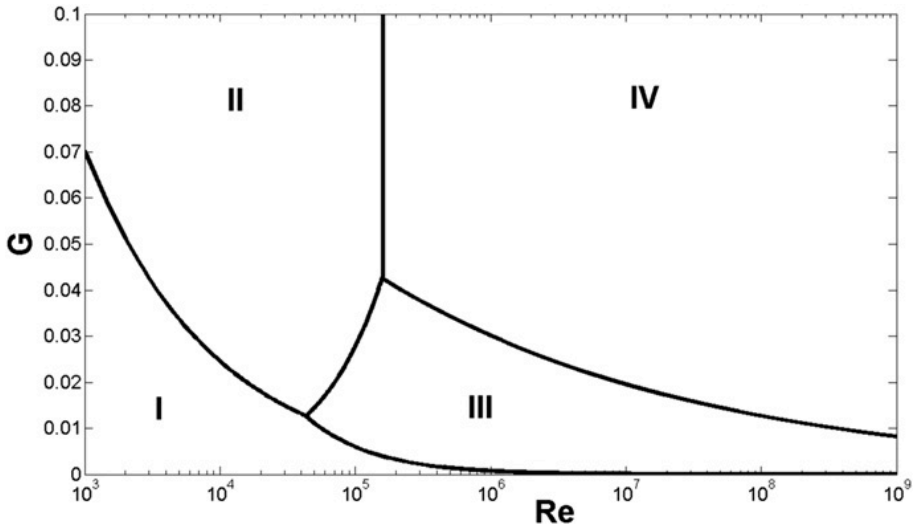

Figure 1.2: The four flow regimes in an enclosed rotor-stator cavity. Merged boundary layers: I (laminar) and III (turbulent). Unmerged boundary layers: II (laminar) and IV (turbulent) [7].

The terminology specific to the rotor-stator cavity literature will be adopted in this paper. The rotor and stator boundary layers are referred to as the Ekman and Bödewadt layers respectively, as a tribute to two of the pioneers of this field. The merged and separated boundary layer regimes are called the Stewartson and the Batchelor flow, respectively.

CHAPTER 2

Literature Review

Poncet et. al. has performed analytical, experimental and numerical work on the closed rotor-stator cavity, with the exception of [10] in which, although the cavity remains without through flow, measurements and simulations were performed on both shrouded and unshrouded cavities. He used the three main approach to simulate the system: RANS, LES and DNS. In this section, Poncet's work on the closed rotor-stator cavity has been divided according to those three numerical approach.

2.1 RANS simulations

The only work with RANS has been done by Nour, Poncet, Debuchy and Bois [10]. In this paper, they performed a analytical, experimental and numerical investigation of turbulent air flow in a rotor-stator system. As mentioned above, the shroud of the rotor-stator is removable. The geometry used in this work is shown below.

In this study, H and Ω, the inter-disk space and the rotational velocity of the rotor, are fixed to 30 mm and 1500 rpm, respectively. Thus, the significant dimensionless parameters of the problem, which are the axial ratio of the cavity $G = H/R$ and the Reynolds number Re_Ω remain constant at 0.08 and 1.47x10^6, respectively. Two values of the geometrical parameter λ, defined by $\lambda = \dfrac{\Delta R}{H}$, are tested on the shrouded case: $\lambda = 0$ and $\lambda = 0.27$, while it remains fixed at $\lambda = 0.27$ for the unshrouded case.

The system studied shows several complexities for a numerical simulation, including

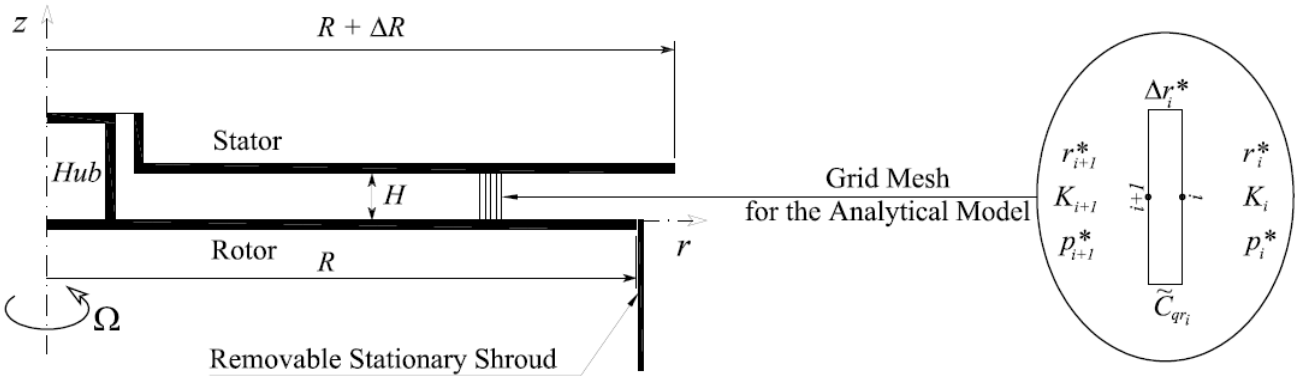

Figure 2.1: System geometry for [10]

high rotation rate, wall effects and transition zones, which are a severe test for turbulence modeling methods. The computational approach is based on a finite volume method using staggered grids for mean velocity components with an axisymmetry hypothesis in the mean. The authors' approach in this study are based on a one-point statistical modeling using a low Reynolds number second-order full stress transport closure derived from the Launder and Tselepidakis model [11] and sensitised to rotational effects by Elena and Schiestel [12]. Poncet et al. investigated these numerical methods on the rotor stator system in a previous study and found it to be adequate for such flow configuration [13]. Comparaisons between, on one hand the shrouded and unshrouded configurations, and on the other hand the experimental and numerical results are shown below in figures 2.2 and 2.3, respectively. The non-dimensional tangential and radial velocities are defined in equation (2.1):

$$V_\theta^* = \frac{V_\theta}{\Omega r} \qquad V_r = \frac{V_r}{\Omega r} \tag{2.1}$$

In figure 2.2, the authors noted that for a radius $r* < 0.613$, the radial flow circulates only through the boundary layers while for $r* \geq 0.773$, the radial exchange of fluid also happens in the core region. Also, the dimensionless tangential velocity in the central core is a decreasing function of r^* until it reaches a constant value for $r* \leq 0.533$. The central core flow rotates as a solid body with a velocity approximately equal to 38-40% of the local

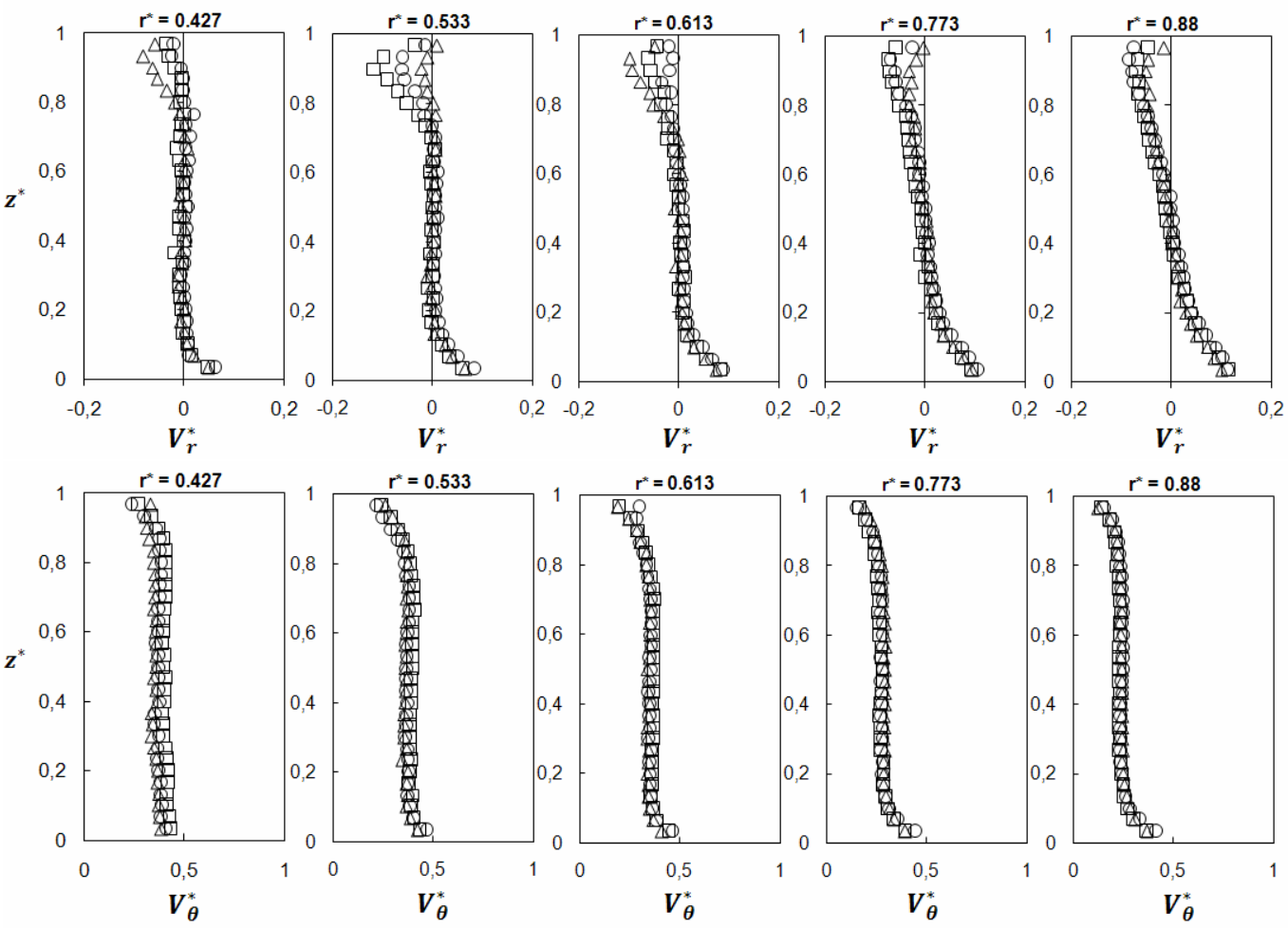

Figure 2.2: Axial profiles of the mean radial and tangential velocity components at various radii. Shrouded configuration: $\lambda = 0$ (◯), $\lambda = 0.27$ (□); Unshrouded configuration: (△) [10].

velocity of the rotating disk.

In figre 2.3, the authors observe a good agreement between the experimental and numerical results, especially at the periphery of the cavity. The three distinct zones of the flow are well observed for both cases. Although the Ekman layer along the rotor is well reproduced by the model, a small discrepancy is observed along the stator, where the RSM model tends to underestimate the thickness of the Bödewadt layer.

For the analytical derivation, the authors assumed the flow to be incompressible, axisym-

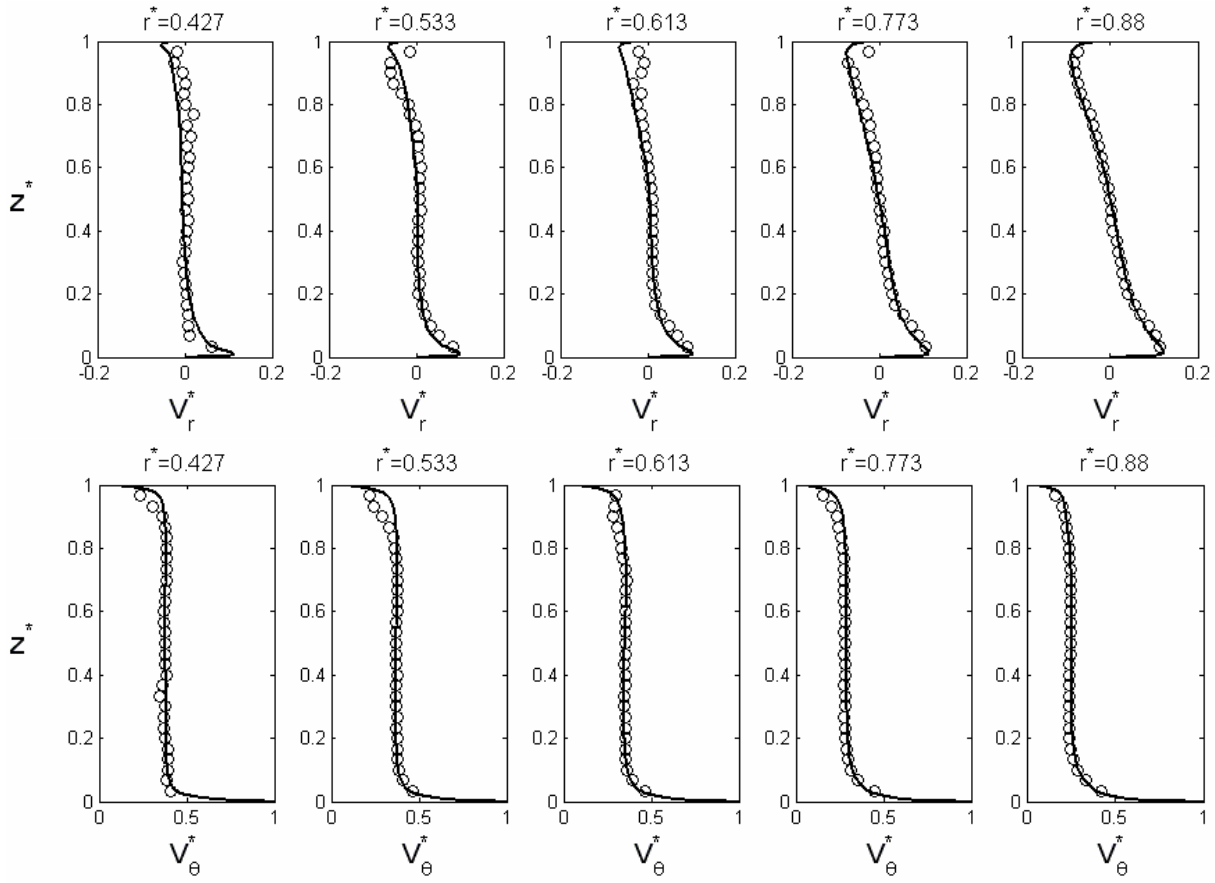

Figure 2.3: Axial profiles of the mean radial and tangential components for the enshrouded case. Experimental results: (◯); numerical results (lines) [10]

metric with negligible turbulence effects, and $G << 1, Re >> 1$. Since this paper focuses on numerical methods, the derivation will not be shown here but the reader is encouraged to refer himself to [10] for more details. The authors found an expression for the core swirl coefficient K, defined by $K = \dfrac{V_\theta}{\Omega}$, as a function of the core swirl coefficient corresponding to the solid body rotation K_B. Introducing the boundary condition $K = K_P$ at $r^* = 1$ [10]:

$$\frac{K}{K_P} = \left(\frac{K_P}{K_B}\right)\left(\frac{K - K_P}{K_B - K_P}\right)^{ar^*} \tag{2.2}$$

This model was compared to the results obtained both experimentally and numerically for the case of the unshrouded rotor-stator cavity. The comparison is shown in figure 2.4.

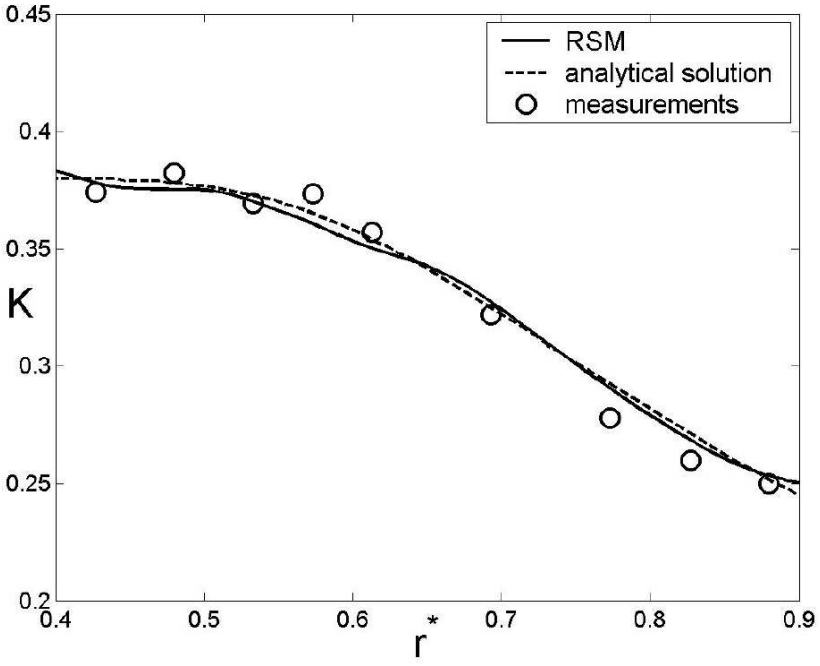

Figure 2.4: Radial distribution of the core swirl ratio [10]

The theoretical distribution is obtained from (2.2) with $K_B = 0.382$, $K_P = 0.22$ and a = 0.6. The authors note that the three results are in very good agreement for this range of radial location. The core swirl coefficient increases when approaching the axis of rotation until it reaches a constant value of 0.382 for $r^* < 0.5$. The authors attribute this variation to the opening at the periphery which strongly modifies the inlet/outlet conditions.

2.2 Large Eddy Simulations

Poncet has also done numerical simulations on the closed rotor-stator cavity using high-order LES. The author simulated the system using the Spectral Vanishing Viscosity approach on a rotor-stator configuration shown in figure 1.1 with and without heat transfer [14], [16]. In another work, he compares two high-order LES methods with an RSM model and previous experimental work [17].

The LES approach consists of a pseudospectral method based on a collocation-Chebyshev

method in the r and z non-homogeneous directions and a Galerkin-Fourier method in the azimuthal periodic direction θ [14], [16]. The time scheme is semi-implicit and second order accurate. It is a combination of an explicit treatment of the convective terms and an implicit treatment for the diffusive terms using the Adams-Bashforth and second-order backward Euler scheme, respectively. The Spectral Vanishing Viscosity approach (SVV), first introduced by Tadmor [18] for stabilizing the inviscid Bürger equation, is incorporated into the governing equations. It was shown by the author that this technique leads to stable discretizations without sacrificing the formal accuracy of the spectral approximation [14].

Referring to figure 1.1, the geometrical parameters used for this simulations are defined as follows:

$$G = \frac{b-a}{h} = 5\,; \quad R_m = \frac{b+a}{b+a} = 1.8\,; \quad 10^5 \leq Re = \frac{\Omega b^2}{\nu} \geq 10^6 \tag{2.3}$$

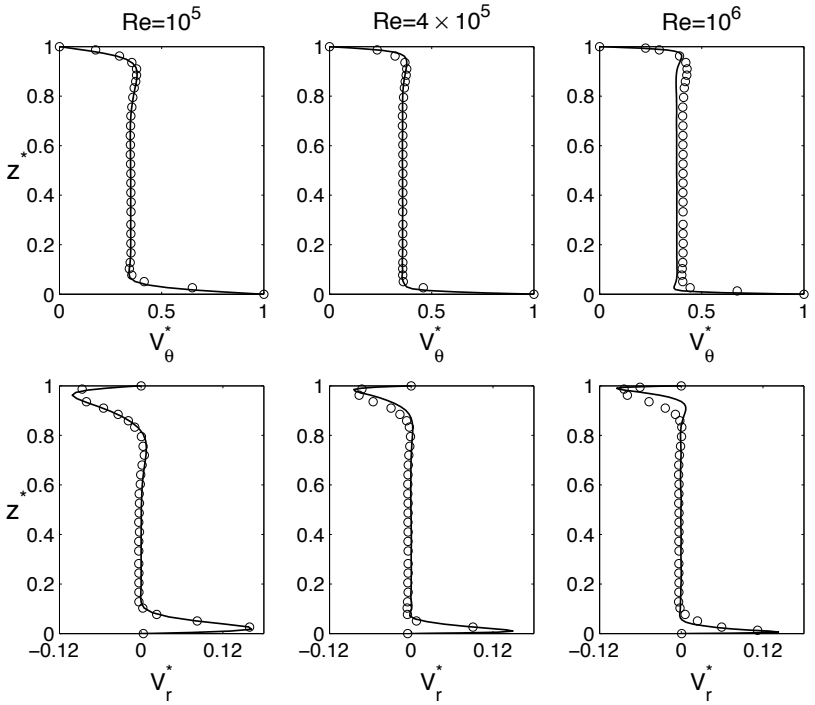

Figure 2.5: Mean velocity profiles at different Reynolds number at $r^* = 0.5$ [14]

Figure 2.5 and 2.6 show the velocity profiles V_θ and V_r and the Reynolds stresses for different Reynolds number. R^*_{rr} and $R^*_{\theta\theta}$ are defined below:

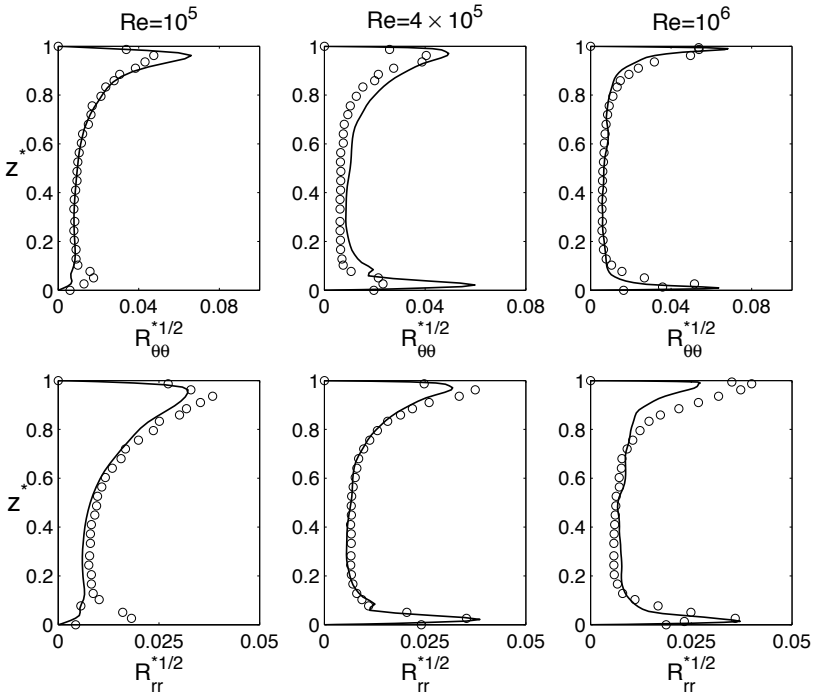

Figure 2.6: Mean axial profiles of the non-dimensional radial and tangential Reynolds stress tensor components R^*_{rr} and $R^*_{\theta\theta}$ at different Reynolds number at $r^* = 0.5$. Comparisons between the LES (-) and experimental ($\circ$) results [14]

$$R^*_{rr} = \frac{\overline{v'^2_r}}{(\Omega r)^2} \qquad R^*_{\theta\theta} = \frac{\overline{v'^2_\theta}}{(\Omega r)^2} \tag{2.4}$$

Whatever the Reynolds number, the mean flows correspond to separated boundary layer flows, belonging to the regime IV denoted by Daily and Nece [7]. There is a good agreement between the experimental and numerical results, although some discrepancies appear at Re $= 10^6$. On both disks, the boundary layer thickness decreases with increasing Reynolds number. Table 2.1 summarises the results obtained by Poncet et. al. [14]. δ_E and δ_B refer to the Ekman and Bödewadt boundary layers, located on the rotor and stator, respectively. Once again, K refers to the entrainment coefficient of the core region located between the two boundary layers.

The swirl coefficient K increases slightly with the Reynolds number. The increase of the rotational velocity of the rotor is primordially felt in the boundary layers rather that

Reynolds number	K	δ_E/h	δ_B/h
10^5	0.35	0.104	0.222
4x10^4	0.36	0.071	0.147
10^6	0.38	0.055	0.084

Table 2.1: Influence of the Reynolds number on the entrainment coefficient K and the boundary layers' thickness for $r^* = 0.5$ [14]

the core region of the flow. The authors stipulate that the boundary layers are known to behave like that of a infinite plate in a moving fluid, namely in this case $\sqrt{\frac{\nu}{\Omega}}$. Although the Bödewadt layer δ_B seems to be in agreement with that hypothesis, the thickness of the Ekman boundary layer δ_E, decreases by a factor of 2 between Re = 10^5 and Re = 10^6. This is characteristic of a rotating boundary layer which becomes turbulent. This is confirmed by the Reynods' stress results shown in figure 2.6: the bödewadt layer is turbulent at all Reynolds number while the Ekman layer becomes turbulent at Re = 4x10^5. The maximum error of the LES results occurs in the prediction of the peak values. At Re = 10^6 for R_{rr}, the experimental data shows the turbulent intensities of the two boundary layers to be equal, while LES predicts the rotor to reach higher turbulence. Poncet explains that such behaviour may come from the anisotropy of the grid, which is globally coarser in the radial direction. Figure 2.7 shows the turbulent intensities at different radii [14].

As expected, the boundary layers become more turbulent with increasing radius. The turbulent intensities therefore depends on the local Reynolds number $Re_r = \frac{\Omega r^2}{\nu}$. Except at $r^* = 0.9$ where the finite cavity effects are no longer negligible, the turbulence intensities remain confined in the two boundary layers. Also, whatever the radial location, the $R^*_{\theta\theta}$ component remain twice as large than R^*_{rr}.

In [17], Viazzo, Poncet et. al. compare different LES models with Reynolds Stress Modelling (RSM) of Elena and Schiestel [12] and the experimental results on a simple closed rotor-stator cavity similar to that shown in figure 1.1. In this study, conservation equations

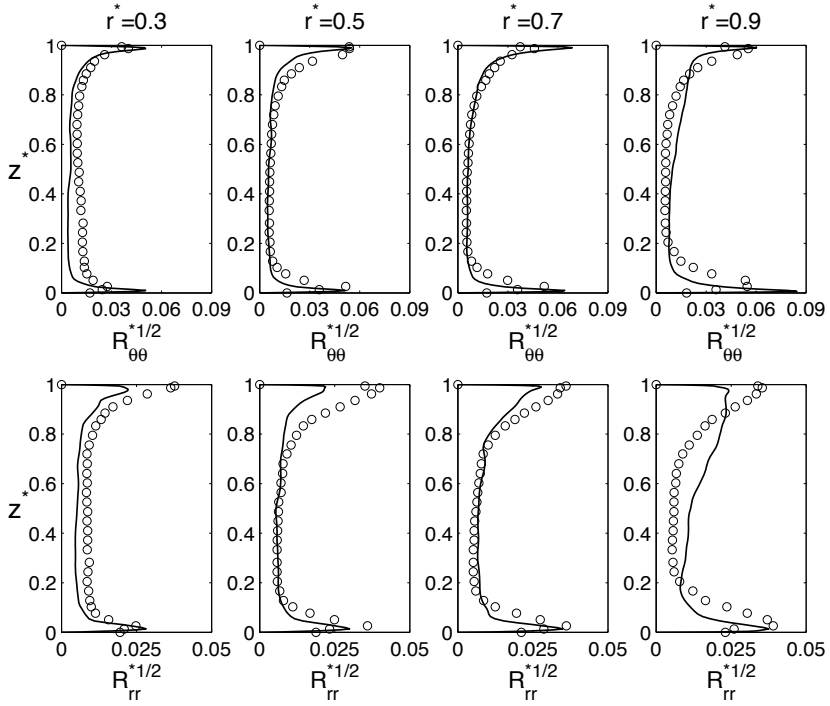

Figure 2.7: Mean axial profiles of the non-dimensional radial and tangential Reynolds stress tensor components R^*_{rr} and $R^*_{\theta\theta}$ at different radii $Re = 10^6$. Comparisons between the LES (-) and experimental ($\circ$) results [14]

are solves using a Fourier approximation in the homogeneous tangential direction. In both non-homogeneous radial and vertical directions, the solutions are approximated using either fourth-order compact finite difference scheme (LES-FD) [19] or a collocation Chebyshev approximation (LES-SVV) [15], similar to the one used in [14]. The reader is encouraged to refer himself to the associated papers for more details. The tangential and radial velocity profiles are shown in figure 2.8.

The agreement between experimental measurements and both LES simulations is satisfactory and furthermore, they provide better overall results than the RSM prediction. Both LES methods slightly underestimate the rotor and stator boundary layers' thickness, especially at large radii for LES-FD. The velocity maxima are well predicted over the stator but greatly overestimated over the rotor. The LES-FD slightly underestimates the core swirl ratio K, predicting a value of K = 0.345 at $r^* = 0.5$ with respect to K = 0.36 obtained by

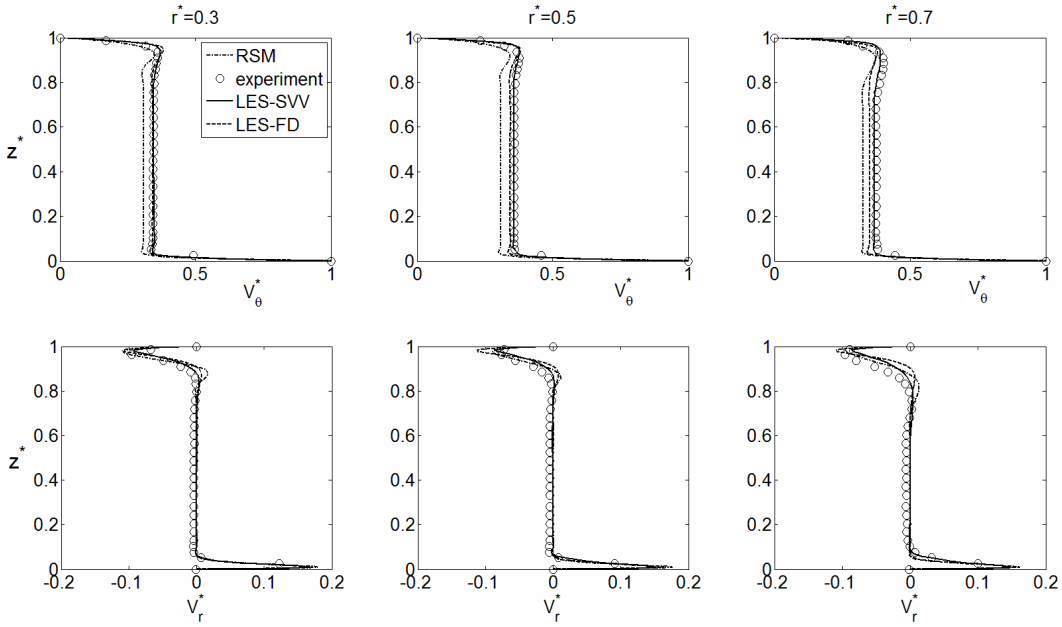

Figure 2.8: Tangential (V_θ) and radial (V_r) velocity profiles at different radii and using different numerical methods.

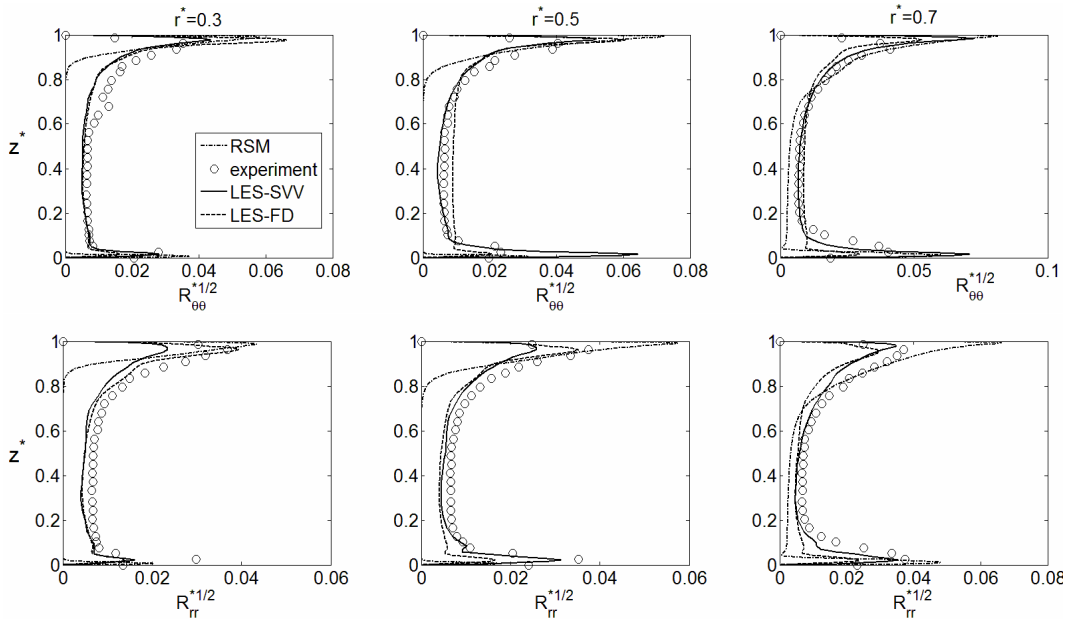

Figure 2.9: Axial variations of two normal Reynolds stress tensor components $R_{\theta\theta}$ and R_{rr} at different radii and using different numerical methods.

LES-SVV and the experimental results. This underestimation is more pronounced by the RSM which predicts K = 0.315.

Second-order statistics available from experimental measurements in the radial and tangential directions have been computed in figure 2.9. The authors point out that the LES simulations provide an overall agreement with the experimental data both in boundary layers and in the core. Note however a slightly better estimation of the turbulence intensity by LES-SVV and LES-FD. On the other hand, RSM seems to strongly overestimate the maxima of the normal components of the Reynolds stress tensor within the stator boundary layer at all radii. Also, it predicts zero stress in the core except at $r^* = 0.7$. The two LES models over predict $R_{\theta\theta}$ in both boundary layers, the maximum being reach by LES-SVV along the stator at $r^* = 0.5$. The leads to a much stronger anisotropy by of the Reynolds stress tensor than in the experiments. The authors suggest that such behaviour could be related to the anisotropy of the grid computation, which is globally much coarser in the tangential direction, especially at large radius.

Overall, the authors agree that both LES methods are well suited for the rotor-stator simulation, while giving a slight preference to the LES-FD simulations due to the odd behaviour to the LES-SVV methods in the boundary layers for the Reynolds' stresses.

2.3 Direct Numerical Simulations

Poncet performed three studies on the rotor-stator configuration shown in figure 1.1 using Direct Numerical Simulation (DNS) [20], [21], [22]. Note however that in these three papers, the z-axis points downward: the rotor and stator are thus respectively located at $z^*=1$ and $z^*=0$. In these publications, the author combined a 3D DNS simulation with a laboratory study to describe the turbulent flow in a closed rotor-stator cavity characterised by a large aspect ratio, G = 18.32. The Reynolds number of this study was set to Re = $9.5\text{x}10^4$, which according to previous studies corresponds to a turbulent stator boundary layer and a laminar

rotor boundary layer.

The author used a pseudospectral collocation-Chebyshev and Fourier method for the spatial discretisation associated with a second order time scheme based on a combination of Adams-Bashforth and backward differentiation formula schemes. The spatial resolution of the grid was set to 300, 80 and 100 in the radial, axial and azimuthal directions respectively. After a statistically steady state was reached, the turbulent characteristics were recorded during 15 time units, which is based on the rotational speed of the rotor, $\tau = \Omega^{-1}$ [20], [21], [22].

Figure 2.10 shows the axial profiles of the mean tangential and radial velocity, V_θ^* and V_r^* at four radial locations [21]. The flow exhibits a typical Batchelor behaviour, similar to the regime IV of Daily and Nece [7]: two developed boundary layers separated by a central rotating inviscid core. The two disks' boundary layer is defined by the axial coordinate at which its velocity reaches 0.99K, where K is the rotational speed of the core. The author states that the stator boundary layer's layer thickness is a decreasing function of radius r*. However, the rotor boundary layer's thickness remains constant independently of r*, which is characteristic of laminar flows. The entrainment coefficient K varies between 0.375 and 0.418 in the radial range considered. It is to be compared to the theoretical value of 0.431 obtained by Owen and Rogers [9] and the semi-empirical value of 0.438 found by Poncet et al. [23].

A polar plot of the mean radial and tangential velocity components is shown in figure 2.11. The DNS results are compared to the experimental results obtained by the authors as well as results from Lygren and Andersson [24] and Von Karman's laminar solution [1]. The polar profile of the stator side, where the radial velocity is negative, falls between the typical fully turbulent behaviour and the laminar solution from the Von Karman similarity solution. The polar plot of the rotor boundary layer is very close to the laminar solution. This confirms the laminar nature of the flow next to the rotor while the turbulence is concentrated on the stator side.

Comparisons between measurements and numerical results of the Reynolds stress vari-

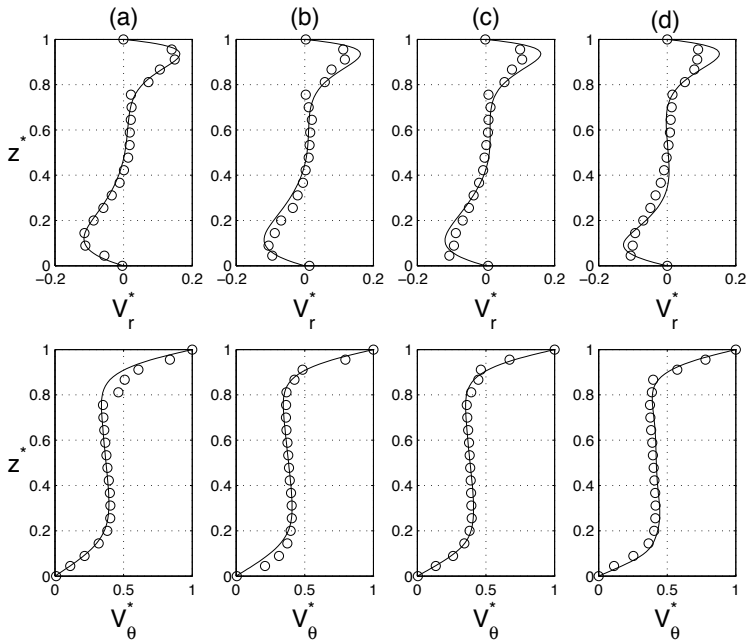

Figure 2.10: Tangential (V_θ^*) and radial (V_r^*) velocity profiles at: (a) r* = 0.44, (b) r* = 0.56, (c) r* = 0.68, (d) r* = 0.80 [21].

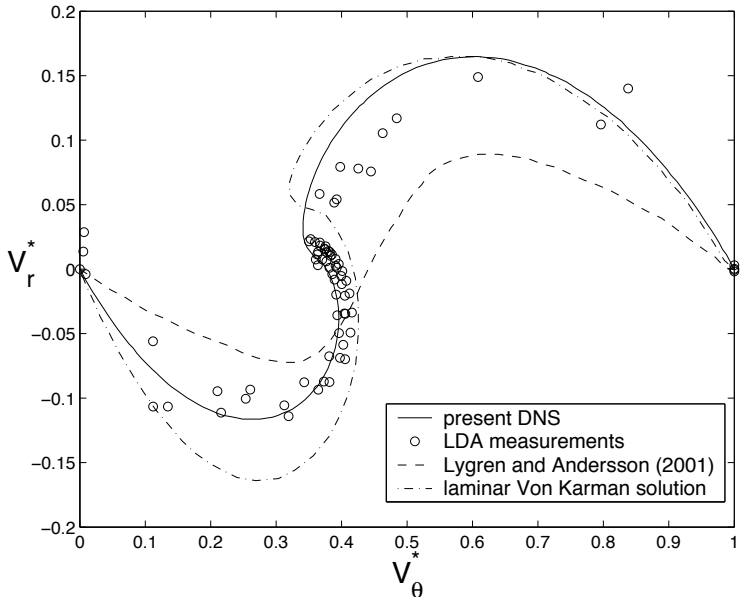

Figure 2.11: Polar plot of the non-dimensional velocity [21]

ations along the radius are shown in figure 2.12. The axial profiles of the Reynolds shear stress $R_{\theta r}^*$ are nearly zero except close to the stator, implying that the reynolds shear stress

is concentrated in the stator boundary layer. The intensities of the normal stresses are also mostly concentrated in the stator boundary layer. This indicates that at this rotation rate, Re = 9.5x10^4, the rotor boundary layer remains laminar. Also, the experimental results show that the flow along the stator becomes more turbulent at large radius, although the numerical simulation does not seem to capture this variation.

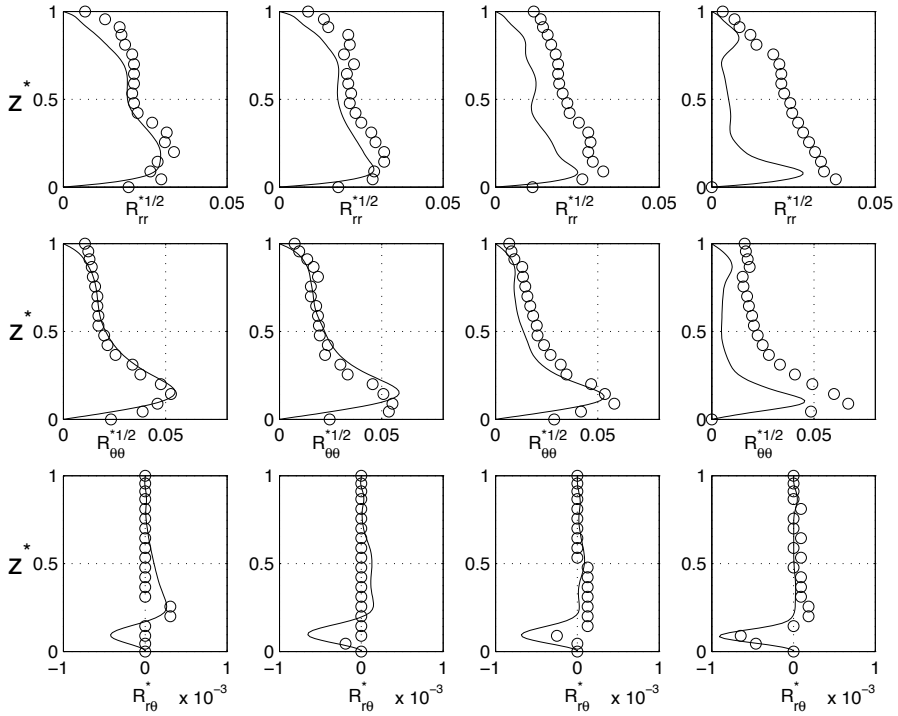

Figure 2.12: Tangential ($R^*_{\theta\theta}$), radial (R^*_{rr}) and shear ($R^*_{r\theta}$) stress profiles at: (a) r* = 0.44, (b) r* = 0.56, (c) r* = 0.68, (d) r* = 0.80 [21].

Figure 2.13 shows the isocontour of the turbulent Reynolds number and kinetic energy defined as such:

$$Re_t = \frac{k^2}{\nu\epsilon} \qquad k^* = \frac{k}{(\Omega b)^2} \tag{2.5}$$

Figure 2.13 confirms that the rotor boundary layer remains laminar [21]. Also, the turbulent intensities are strongest at large radius and decrease as the fluid flows inward. The presence of isocontours close to the junction between the stationary disk and the shroud

suggest that the turbulence may start to develop in this zone. Also, as expected, the low value of the maximum turbulent Reynolds number $\mathrm{Re}_t = 20.52$ confirms the weakly turbulent nature of this flow.

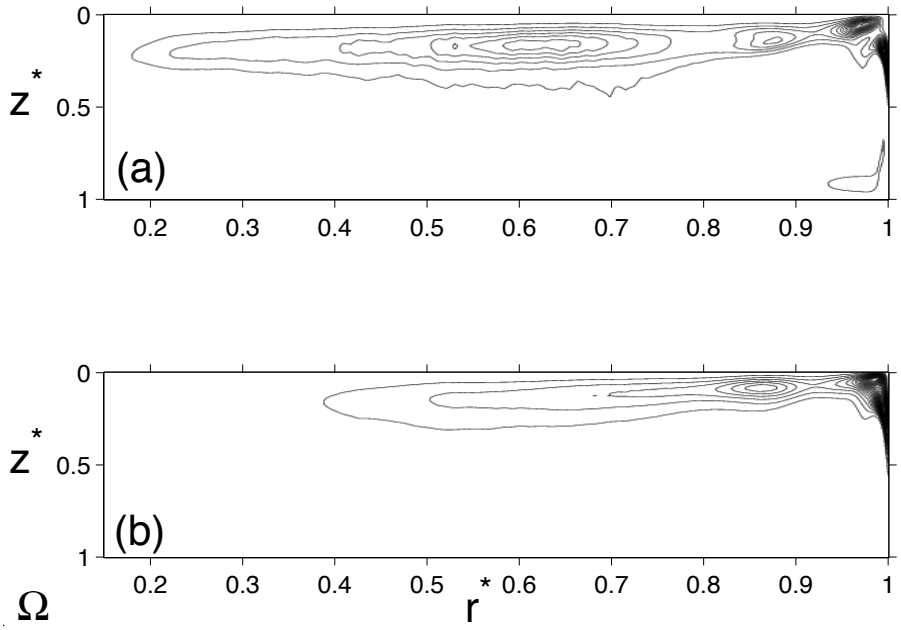

Figure 2.13: Regularly spaced isocontours of: (a) the turbulent Reynolds number $0 < \mathrm{Re}_t \leq 20.52$; (b) the turbulent kinetic energy $0 \leq \mathrm{k}^* \leq 1.377\mathrm{x}10^{-2}$ [21]

CHAPTER 3

Governing Equations and Methodology

3.1 Governing equations

In this section are presented the governing equations that are used by the software AVBP. The equations below are the ones solved by AVBP regardless of the assumptions made by a specific simulation. For example, the flow in a simulation cannot be specified as incompressible, the incompressibility of the flow is a consequence of the governing equations. Therefore the equations are presented in their most general form, as they are treated by AVBP.

In the following sections, unless specified otherwise, the Einstein's index notation will be implied in repeated indices. Note however that the index k refers to the k^{th} species and does not follow the summation rule.

3.1.1 Navier-Stokes Equations

The dynamical behavior of a fluid element is determined by three conservation laws: the conservation of mass, momentum and energy. In differential form, the general form of the conservation laws are given as follows:

$$\frac{\partial \rho_k}{\partial t} + \frac{\partial}{\partial x_j}(\rho_k u_i) = -\frac{\partial}{\partial x_j}\left[J_{j,k}\right] + \dot{\omega} \tag{3.1}$$

$$\frac{\partial \rho u_i}{\partial t} + \frac{\partial}{\partial x_i}(\rho u_i u_j) = -\frac{\partial}{\partial x_j}[P\delta_{ij} - \tau_{ij}] \tag{3.2}$$

$$\frac{\partial \rho E}{\partial t} + \frac{\partial}{\partial x_j}(\rho E u_j) = -\frac{\partial}{\partial x_j}[u_i(P\delta_{ij} - \tau_{ij}) + q_j] + \dot{\omega}_T + Q_r \tag{3.3}$$

where ρ is the fluid density, u_i the i^{th}velocity component, P the pressure and E the total energy. The stress tensor is given by τ_{ij}, δ_{ij} is the Kronecker delta and q_j the heat flux. The

source terms $\dot{\omega}$, $\dot{\omega}_T$ and Q_r are the mass, chemical and radiative source terms.

It is conventional to express the governing equations in terms of the conservative variables vector, $\boldsymbol{U}$ defined below:

$$\boldsymbol{U} = \begin{bmatrix} \rho_k \\ \rho u_i \\ \rho E \end{bmatrix} \tag{3.4}$$

Therefore, in terms of the vector $\boldsymbol{U}$ the conservation laws can be written as:

$$\frac{\partial \boldsymbol{U}}{\partial t} + \frac{\partial}{\partial x_j}(\boldsymbol{F_c} - \boldsymbol{F_v}) = \boldsymbol{Q} \tag{3.5}$$

where $\boldsymbol{Q}$ is the source term, $\boldsymbol{F_c}$ and $\boldsymbol{F_v}$ the convective (or inviscid) and viscous flux terms, respectively. They are defined as follows:

$$\boldsymbol{Q} = \begin{bmatrix} \dot{\omega}_k \\ 0 \\ \dot{\omega}_T + Q_r \end{bmatrix}, \quad \boldsymbol{F_c} = \begin{bmatrix} \rho_k u_j \\ \rho u_i u_j + P\delta_{ij} \\ (\rho E + P\delta ij)u_j \end{bmatrix}, \quad \boldsymbol{F_v} = \begin{bmatrix} J_{j,k} \\ -\tau_{ij}u_i + q_j \\ -\tau_{ij} \end{bmatrix} \tag{3.6}$$

AVBP uses a Finite Volume Method for the discretization of the domain space. Therefore, it solves the integral form of equation (3.5). Consider a control volume Ω fixed in space and bounded by a close surface $\partial\Omega$ represented in figure 3.1. We also introduce a surface element dS with an associate outward pointing normal vector $\vec{n}$:

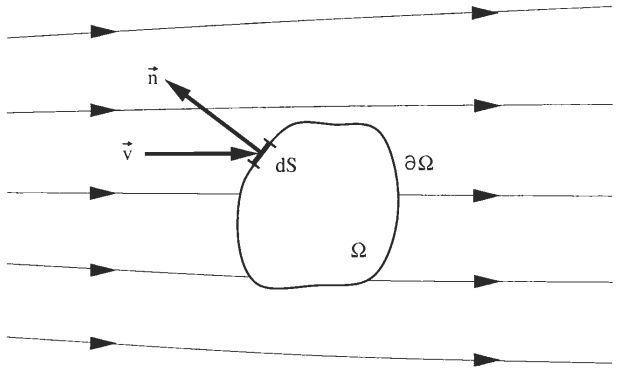

Figure 3.1: Definition of a finite control volume fixed in space

Therefore, following the definition of the control volume Ω, the integral form of the Navier-Stokes equations is given in equation (3.7):

$$\frac{\partial}{\partial t}\int_{\Omega} \boldsymbol{U} + \oint_{\partial\Omega} (\boldsymbol{F_c} - \boldsymbol{F_v})\mathrm{dS} = \int_{\Omega} \boldsymbol{Q}\mathrm{d}\Omega \tag{3.7}$$

3.1.2 Thermodynamic Equations

There are two more equations required for the system to be well posed, as the pressure and temperature remain to be solved for. AVBP deals strictly with gaseous flow; therefore the equation of state for an ideal gas is used:

$$P = \rho\, r_g\, T \tag{3.8}$$

where r_g is the gas constant of the mixture, $r_g = R/W$, R being the universal gas constant and W the molecule weight of the mixture. It is given by equation (3.9):

$$\frac{1}{W} = \sum_{k=1}^{N} \frac{Y_k}{W_k} \tag{3.9}$$

where Y_k is the mass fraction of the k^{th} species.

The last equation relates the total energy E and the temperature. The standard reference state used is:

$$P_o = 1 \text{ bar}, \quad T_o = 0 \text{ K} \tag{3.10}$$

AVBP uses a table listing of the sensible enthalpies from 0 K to 5000 K in a 100 K interval. Therefore the sensible enthalpy can be evaluated using the following equation:

$$h_{s,k}(T_i) = \int_{T_o}^{T_i} C_{p,k}\, \mathrm{d}T = \frac{h^m_{s,k}(T_i) - h^m_{s,k}(T_o)}{W_k} \tag{3.11}$$

$h_{s,k}(T_i)$ is defined as the sensible enthalpy at temperature T_i, $C_{p,k}$ the mass heat capacity at constant pressure and $h^m_{s,k}$ the molar sensible enthalpy. The subscript k refers to the k^{th} species as it will for all variables in this section. Using equation (3.11), the sensible energy

can be calculated using equation (3.13):

$$e_{s,k}(T_i) = \int_{T_o}^{T_i} C_{v,k}\,\mathrm{d}T = h_{s,k}(T_i) - rT_i \tag{3.12}$$

$$= h_{s,k}(T_i) - \frac{p}{\rho} \tag{3.13}$$

where $e_{s,k}(T_i)$ is the sensible energy at temperature T_i and $C_{v,k}$ the mass heat capacity at constant volume. The ideal gas law was used to derive equation (3.13). Finally, the total energy E can be related to the sensible energy by (3.14):

$$E(T_i) = \sum_{k=1}^{N} e_{s,k}(T_i) + \frac{1}{2}u_j u_j \tag{3.14}$$

herefore, the pressure and temperature can be obtained from the conservative variables using the combined equations (3.8), (3.11), (3.13) and (3.14).

3.2 The Large Eddy Simulation Approach

3.2.1 The LES Concept

Turbulence is a natural phenomenon of fluid mechanics and is due to the non-linear convective terms in the Navier-Stokes equation (3.3). The main issue in numerically reproducing a turbulent flow is that it contains vortices of very large different sizes.

Direct Numerical Simulation (DNS) calculates directly the Navier-Stokes equations as is, without modeling any part of the structures' spectrum. The solution is therefore exact. However, the mesh size is dictated by the smallest turbulent structures. Their size is given by Kolmogorov scales η:

$$\eta = \left(\frac{\nu^3}{\epsilon}\right)^{1/2} \tag{3.15}$$

where ϵ is the rate of dissipation of the kinetic turbulent energy per unit mass, and ν the kinematic viscosity of the fluid. There is an energy cascade from large vortices to smaller vortices. The structures with characteristic sizes η are then directly dissipated by the fluid's viscosity. As a result, to capture all the turbulent kinetic energy of the flow, the mesh size is proportional to $N = Re^{9/4}$, which is much to large for today's computer to handle except for very simple, academic geometries. The alternative is to calculate only a part of the flow and model the other. The most used modeling methods today use the Reynolds-Averaged Navier-Stokes (RANS) equations and the Large Eddy Simulation (LES).

The RANS equations are time-averaged equations of motion. These equations give approximate averaged-solutions to the Navier-Stokes equations. All of the turbulent structures are modeled. LES stands between RANS and DNS, as it calculates directly the large scale structures that contain most of the turbulent kinetic energy and models the smaller ones. The small scales vortices are modeled by a algebraic subgrid-scale (SGS) turbulent model. LES is less sensitive to models than the RANS equations but require less dissipative schemes in order to capture correctly the energy cascade. The RANS, LES and DNS properties are summarized in Figure 3.2 [25]:

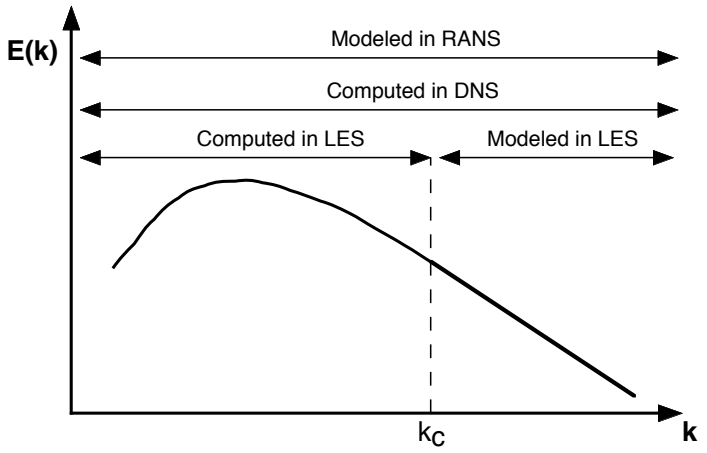

Figure 3.2: Turbulence energy spectrum plotted as a function of wave numbers. RANS, LES and DNS are summarized in terms of spatial frequency range. k_c is the cut-off wave number used in LES (log-log diagram).

LES is nowadays recognized as an intermediate approach in comparison to the now classical RANS methods. This is especially true for industrial applications where an understanding of the unsteady aspect of the flow is essential.

From a mathematical perspective, the major difference between LES and RANS comes from the operator employed in the derivation of each methods' governing equation. In RANS, the operator consist of a temporal or ensemble average over a set of realization of the studies. The enclosed terms are representative of the physics taking place of over the entire range of frequencies present in the ensemble of realization under consideration.

In LES, the operator is a spatially localized time independent filter of given size, Δ, to be applied to a single realization of the studied flow. Resulting from this spatial average is a separation between the scales larger and smaller than the filter size. The unclosed terms in LES are representative of the physics associated with the small structures with high frequencies present in the flow. Due to the filtering approach, LES allows a dynamic representation of the large scale motions whose contributions are critical in complex geometries. The LES predictions of complex turbulent flows are therefore closer to the physics than the RANS predictions since large scale phenomena such as large vortex shedding and acoustic waves are

embedded in the set of governing equations (3.18). Figure 3.3 illustrates the results obtained by the three different numerical approach, RANS, LES and DNS [25]:

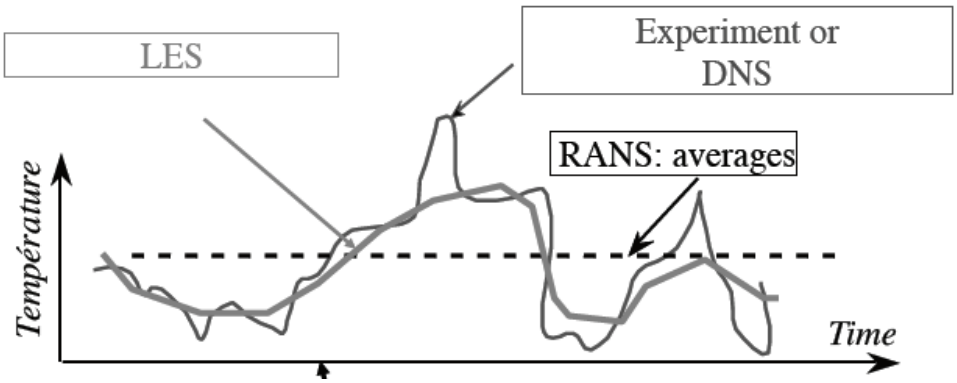

Figure 3.3: Results comparisons obtained with RANS, LES and DNS.

For the reasons presented above, LES has a clear potential in predicting turbulent flows encountered in industrial applications. The accuracy of the solution depends on the size of the spectrum that is being model and therefore the filter size Δ.

3.2.2 The Governing Equation for LES

In LES, variables are filtered either in spectral space, where components greater than a given cut-off frequency are suppressed, or in physical space where the variables are weighted average over a given volume. The filtered quantity f is defined as [25]:

$$\bar{f}(x) = \int f(x')F(x - x')\mathrm{d}x' \tag{3.16}$$

where F is the LES filter. A mass-weighted Favre filtering is then introduced according to the definition given in equation (3.17):

$$\bar{\rho}\tilde{f} = \int \rho f(x')F(x - x')\mathrm{d}x' \tag{3.17}$$

The filtered quantity is resolved in the numerical simulation whereas $f' = f$ - $\bar{f}$ corresponds to the unresolved part, the subgrid scale term due to unresolved motion. The governing equations for LES are obtained by filtering the instantaneous balance equations,

which lead to the following:

$$\frac{\partial}{\partial t}\int_{\Omega}\tilde{\boldsymbol{U}}+\oint_{\partial\Omega}(\tilde{\boldsymbol{F_c}}-\tilde{\boldsymbol{F_v}})\mathrm{dS}=\int_{\Omega}\tilde{\boldsymbol{Q}}\mathrm{d}\Omega+\oint_{\partial\Omega}\boldsymbol{S^t}\mathrm{dS} \tag{3.18}$$

where, as in the regular Navier-Stokes equations, the vector $\tilde{\boldsymbol{U}}$ is the conservative variable, $\tilde{\boldsymbol{Q}}$ the source term and $\tilde{\boldsymbol{F_c}}$ and $\tilde{\boldsymbol{F_v}}$ correspond to the inviscid and viscous flux terms. These variables are defined below:

$$\tilde{\boldsymbol{U}}=\begin{bmatrix}\bar{\rho}_k\\ \bar{\rho}\tilde{u}_i\\ \bar{\rho}\tilde{E}\end{bmatrix},\quad \tilde{\boldsymbol{Q}}=\begin{bmatrix}\bar{\dot{\omega}}_k\\ 0\\ \bar{\dot{\omega}}_T+\bar{Q}_r\end{bmatrix},\quad \tilde{\boldsymbol{F_c}}=\begin{bmatrix}\bar{\rho}_k\tilde{u}_j\\ \bar{\rho}\tilde{u}_i\tilde{u}_j+\bar{P}\delta_{ij}\\ (\bar{\rho}\tilde{E}+\bar{P}\delta ij)\tilde{u}_j\end{bmatrix},\quad \tilde{\boldsymbol{F_v}}=\begin{bmatrix}\bar{J}_{j,k}\\ -\overline{\tau_{ij}u_i}+\bar{q}_j\\ -\tau_{ij}\end{bmatrix} \tag{3.19}$$

The additional term $\boldsymbol{S^t}$ in equation (3.18) is the subgrid scale or turbulent flux term introduced by the filtration process done for the LES methodology. It is defined in equation (3.20):

$$\boldsymbol{S^t}=\begin{bmatrix}\bar{J}^t_{j,k}\\ \bar{q}^t_j\\ -\bar{\tau}^t_{ij}\end{bmatrix} \tag{3.20}$$

The vector $\boldsymbol{S^t}$ introduces a closure problem as each of its element is a non-linear fluctuation that cannot be directly calculated. Therefore, a model needs to be supplied for each of these term. Only the quantity $\bar{\tau}^t_{ij}$ will be discussed below as the other terms, set to zero in the rotor-stator simulations, are irrelevant in this paper.

3.2.3 Viscosity Models

The LES method depends on the filter size Δ and the LES model used for the turbulent for the turbulent viscosity ν_t.

These models are derived assuming that the corresponding LES filter Δ is independent on time and space. Therefore, the variations in the filter size due to a non-uniform or moving mesh are not directly accounted for in the derivation of the LES models. However, the

change of cell topology is still taken into account through the local cell volume according to equation (3.21):

$$\Delta = V_{cell}^{1/3} \tag{3.21}$$

The filtered compressible Navier-Stokes equations exhibit SGS tensors and vectors describing the interaction between non-resolved and resolved motion. This interaction is accounted for through the introduction of the turbulent viscosity. Such an approach assumes the effect of the SGS field on the resolved field to be purely dissipative.

As mentioned in the previous section, $\bar{\tau}_{ij}^t$ is the result of the non-linearity term in the Navier-Stokes equations. Its is given by equation (3.23):

$$\bar{\tau}_{ij}^t = -\bar{\rho}\ (\widetilde{u_i u_j} - \tilde{u}_i \tilde{u}_j) \tag{3.22}$$

$$= -2\ \bar{\rho}\ \nu_t \left(\tilde{S}_{ij} - \frac{1}{3}\delta_{ij}\tilde{S}_{kk} \right) \tag{3.23}$$

where $\tilde{S}_{ij}$ the strain rate tensor and is defined by the following equation:

$$\tilde{S}_{ij} = \frac{1}{2}\left(\frac{\partial \tilde{u}_i}{\partial x_j} + \frac{\partial \tilde{u}_j}{\partial x_i} \right) - \frac{1}{3}\delta_{ij}\frac{\partial \tilde{u}_k}{\partial x_k} \tag{3.24}$$

$\tilde{S}_{ij}$ can be directly calculated from the Favre filtered velocity vector. Therefore, the turbulent viscosity ν_t is the only variable that requires modeling for closure. The different LES models used are discussed in the following section.

3.2.3.1 Smagorinsky Subgrid-Scale Model

The Smagorinsky model, named after its author, was the first developed SGS model [26]. It is given by equation (3.25):

$$\nu_t = (C_s \Delta)^2 \sqrt{2\tilde{S}_{ij}\tilde{S}_{ij}} \tag{3.25}$$

C_s is constant dimensionless empirical parameter, called the Smagorinsky coefficient and is set to 0.18. This model has the particularity of supplying the right amount of dissipation

of kinetic energy in homogeneous isotropic flows. However, locality is lost and only global quantities are maintained. It is generally regarded as being too dissipative and is therefore not suited for transitioning flows.

3.2.3.2 WALE Subgrid-Scale Model

The Wall adaptive local eddy-viscosity (WALE) model was developed by Ducros, Nicoud and Poinsot for wall-bounded flows in an attempt to recover the scaling laws of the wall [27]. It is given by the following equations:

$$\nu_t = (C_w \Delta)^2 \frac{\left(S_{ij}^d S_{ij}^d\right)^{3/2}}{\left(\tilde{S}_{ij}\tilde{S}_{ij}\right)^{5/2} + \left(S_{ij}^d S_{ij}^d\right)^{5/4}} \tag{3.26}$$

where $C_w^2 \approx 10.6 C_s^2$. For reasons connected to the wall behavior of the SGS model, a new operator S_{ij}^d based on the traceless symmetric part of the square of the gradient velocity tensor $\bar{g}_{ij}$, was defined [27]:

$$s_{ij}^d = \frac{1}{2}\left(\tilde{g}_{ij}^2 + \tilde{g}_{ji}^2\right) - \frac{1}{3}\tilde{g}_{kk}^2 \delta_{ij} \tag{3.27}$$

$$\bar{g}_{kk} = \frac{\partial \bar{u}_{ij}}{\partial x_j} \tag{3.28}$$

where $\bar{g}_{ij}^2 = \bar{g}_{ik}\bar{g}_{kj}$.

3.3 Numerical Scheme and Discretization Method

In the previous sections, the complete system of governing equations required to solve the fluid problem, along with the viscosity models, was introduced. In this section, the two numerical methods used in the AVBP rotor-stator simulations will be presented. Only the general approach will be introduced here, the reader is encouraged to consult the references for details [28].

AVBP was designed to solve flow problems with complex industrial geometries. It uses unstructured grids to discretize the physical space. The main advantage of the unstructured grids is based on the fact that the tetrahedral grids can be generated efficiently and automatically, independently of the complexity of the domain. However, only low-order methods, generally no higher than 2^{nd} order, can be used with unstructured grids. This deficiency is generally compensated by the large number of nodes used in the discretization of the physical domain.

As mentioned in the previous section, flow solver used for the discretization of the governing equation is based on the Finite Volume (FV) method. This approach utilizes directly the integral form of the Navier-Stokes equations (3.7). AVBP uses the cell-centered approach for implementing the FV method. In this technique, the flow quantities are stored at the grid nodes and the mean value of the fluxes are obtained by averaging along the cell edges.

The mathematical formulation of the numerical methods is presented below in its most general form. The two methods used, the Lax-Wendroff and the Two-setp Taylor Galerkin (TTGC) schemes, were rewritten to comply with the Arbitrary Lagrangian Eulerian methods.

3.3.1 Lax-Wendroff Scheme

$$\boldsymbol{U_i^{n+1}} = \boldsymbol{U_i^n} - \Delta t \frac{V_i^{n+1/2}}{V_i^{n+1}} \left(\boldsymbol{R_i} + \boldsymbol{U_i^n}\right) \tag{3.29}$$

$$\boldsymbol{R_i} = \frac{1}{V_i^{n+1/2}} \sum_{j \,|\, i \,\epsilon\, \Omega_j} V_{\Omega_j}^{n+1/2} \left(D_{i,\Omega_j}^{(1)} \boldsymbol{R_{\Omega_j}} + D_{i,\Omega_j}^{(2)} \left[\boldsymbol{R_{\Omega_j}} + \boldsymbol{R_{\Omega_j}}^c\right]\right) \tag{3.30}$$

$$D_{i,\Omega_j}^{(1)} = \frac{1}{n_v} \tag{3.31}$$

$$D_{i,\Omega_j}^{(2)} = \frac{\delta t_{\Omega_j}}{2 N_d V_{\Omega_j}^{n+1/2}} \left(\boldsymbol{A_{\Omega_j}^n} - \boldsymbol{\dot{X}_{\Omega_j}}\right) \cdot \mathbf{d}\boldsymbol{S_i^{n+1/2}} \tag{3.32}$$

$$\boldsymbol{R_{\Omega_j}} = \frac{1}{N_d V_{\Omega_j}^{n+1/2}} \sum_{i \,|\, i \,\epsilon\, \Omega_j} \left(\boldsymbol{F_i^n} - \boldsymbol{U_i^n} \dot{X}_i\right) \cdot \mathbf{d}\boldsymbol{S_i^{n+1/2}} \tag{3.33}$$

$$\boldsymbol{R_{\Omega_j}^c} = \boldsymbol{U_{\Omega_j}^n} \frac{1}{N_d V_{\Omega_j}^{n+1/2}} \sum_{i \,|\, i \,\epsilon\, \Omega_j} \boldsymbol{\dot{X}_i} \cdot \mathbf{d}\boldsymbol{S_i^{n+1/2}} \tag{3.34}$$

In the above equations, $\boldsymbol{U_i^n}$ one of the four conservative variables -ρu, ρv, ρw or ρe-, n_v the number of vertices of the grid element Ω_j, N_d the number of dimensions, $\boldsymbol{X_i}$ the nodes position and $\dot{X}_i$ their speed [28].

3.3.2 Two Step Taylor Galerkin scheme

The predictor and corrector steps of the two step Taylor Galerkin scheme (TTGC) are given as follows:

$$\boldsymbol{\tilde{U}^n} = \boldsymbol{U^n} - \Delta t \left(\boldsymbol{M^{n+\alpha}}\right)^{-1} \left[\alpha L^{n+\alpha/2}(\boldsymbol{U^n}) + \beta \Delta t L L^{n+\alpha/2}(\boldsymbol{U^n}) + \frac{\boldsymbol{M^{n+\alpha}} - \boldsymbol{M^n}}{\Delta t} \boldsymbol{U^n}\right] \tag{3.35}$$

$$\boldsymbol{\tilde{U}^{n+1}} = \boldsymbol{U^n} - \Delta t \left(\boldsymbol{M^{n+1}}\right)^{-1} \left[L^{n+1/2}(\boldsymbol{\tilde{U}^n}) + \gamma \Delta t L L^{n+1/2}(\boldsymbol{U^n}) + \frac{\boldsymbol{M^{n+1}} - \boldsymbol{M^n}}{\Delta t} \boldsymbol{U^n}\right] \tag{3.36}$$

where $\boldsymbol{M}^{n+\alpha}$ and $\boldsymbol{M}^{n+1}$ are the mass matrices of the predictor and corrector steps, respectively. α, β and γ are constant parameters chosen to regulate the dissipation and dispersion properties of the numerical scheme. The other terms are given by equations given below [28]:

$$L_i^{n+\tau}(\boldsymbol{U}_i^n) = \sum_{j \,|\, i \,\epsilon\, \Omega_j} \frac{V_{\Omega_j}}{n_v} \boldsymbol{R}_{\Omega_j}^{n+\tau} \tag{3.37}$$

$$LL_i^{n+\tau}(\boldsymbol{U}^n) = \frac{1}{N_d} \left[\boldsymbol{A}_{\Omega_j}^n - \dot{\boldsymbol{X}}_{\Omega_j} \right] \left(\boldsymbol{R}_{\Omega_j}^{n+\tau} + (\boldsymbol{R}^c)_{\Omega_j}^{n+\tau} \right) \cdot \mathbf{d}\boldsymbol{S}_i^{n+\tau} \tag{3.38}$$

$$\mathbf{R}_{\Omega_j}^{n+\tau} = \frac{1}{N_d V_{\Omega_j}^{n+\tau}} \sum_{i \,|\, i \epsilon\, \Omega_j} \left(\boldsymbol{F}_i^n - \boldsymbol{U}_i^n \dot{\boldsymbol{X}}_i \right) \cdot \mathbf{d}\boldsymbol{S}_i^{n+\tau} \tag{3.39}$$

$$\mathbf{R}_{\Omega_j}^{n+\tau} = \boldsymbol{U}_{\boldsymbol{\Omega}}^{\boldsymbol{n}} \frac{1}{N_d V_{\Omega_j}^{n+\tau}} \sum_{i \,|\, i \epsilon\, \Omega_j} \dot{\boldsymbol{X}}_i \cdot \mathbf{d}\boldsymbol{S}_i^{n+\tau} \tag{3.40}$$

CHAPTER 4

Results and Discussion

In this section the input parameters, geometric configuration and the mesh used in the AVBP simulation are first discussed. The velocity profiles obtained are then presented, followed by their discussion.

4.1 Meshing and Input Parameters

The Poncet experiment selected to be reproduced numerically in AVBP can be found in [20]. The general geometry used in this study in the same as the one used by Daily and Nece and shown in Figure1.1 [7]. The geometrical parameters are presented in table 4.1.

In Poncet's experiment, water is confined in a closed rotor-stator system. The rotor, located on lower side of the system, is rotated at a fixed velocity. The results are obtained after the flow has statically converged [20]. The geometry used in AVBP is the same. However, the viscosity and the rotor velocity were altered to increase the rate of statistical

Parameter	Value	Units
a	38	mm
b	250	mm
h	11.6	mm
Ω	1.43	rad/s
μ	9.44x10^{-7}	m^2/s

Table 4.1: Geometrical parameters of Poncet's experiment

Parameter	Experiment	AVBP	Units
Ω	1.43	250	rad/s
ν	9.44x10^{-7}	1.79x10^{-4}	m^2/s
Re_Ω	9.5x10^4	9.5x10^4	

Table 4.2: The experimental and simulation parameters

convergence while maintaining the same geometric Reynolds number, defined by (1.1). Since AVBP only deals with gaseous flow, the rotor velocity was increased to the maximum value which allowed the flow to remain incompressible, $0.2a_0$, where a_0 is the speed of sound. A table summarising the geometric and simulation parameters is table 4.2.

Three different meshes were used in the simulations of the rotor-stator systems. The main difference between the grids is the amount of cells used in the thickness of the rotor-stator. The first mesh's resolution is uniform across all directions. It has 14 cells across the geometry's thickness and a total of 17 millions nodes. It will be referred to as "first mesh". It is shown in figure 4.1.

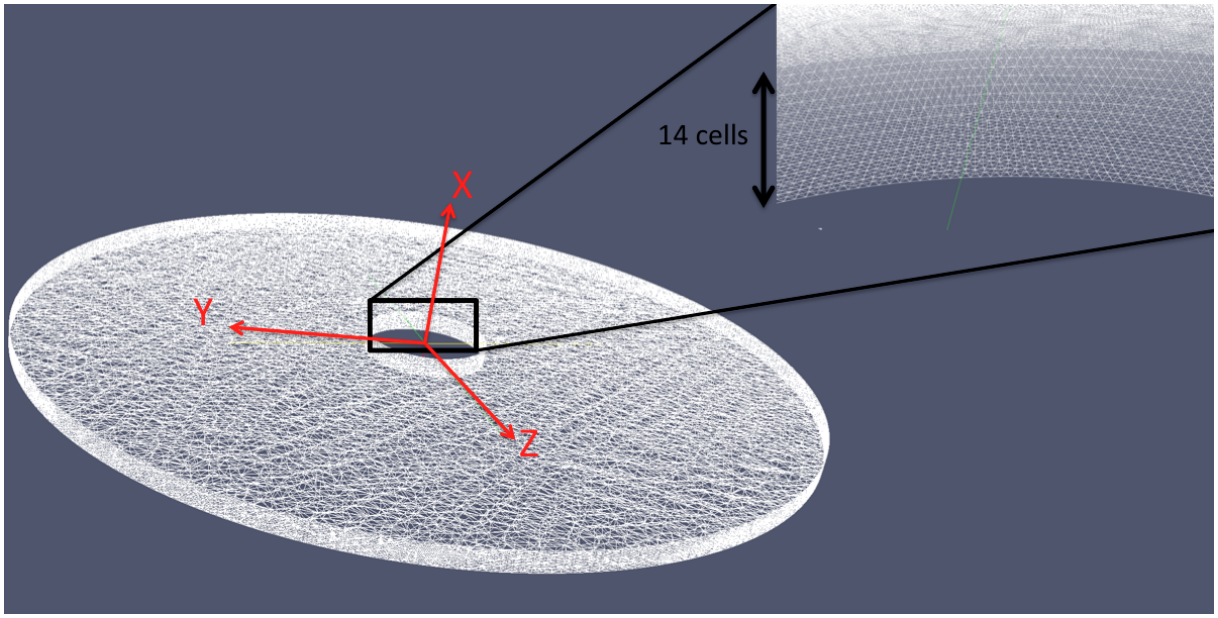

Figure 4.1: First mesh

In the second mesh, the thickness direction was favored over the others to obtain more precise results. It has 35 cells in the thickness' direction and a total of 2.6 millions nodes. It will be referred to as "smart mesh". It is shown in figure 4.2.

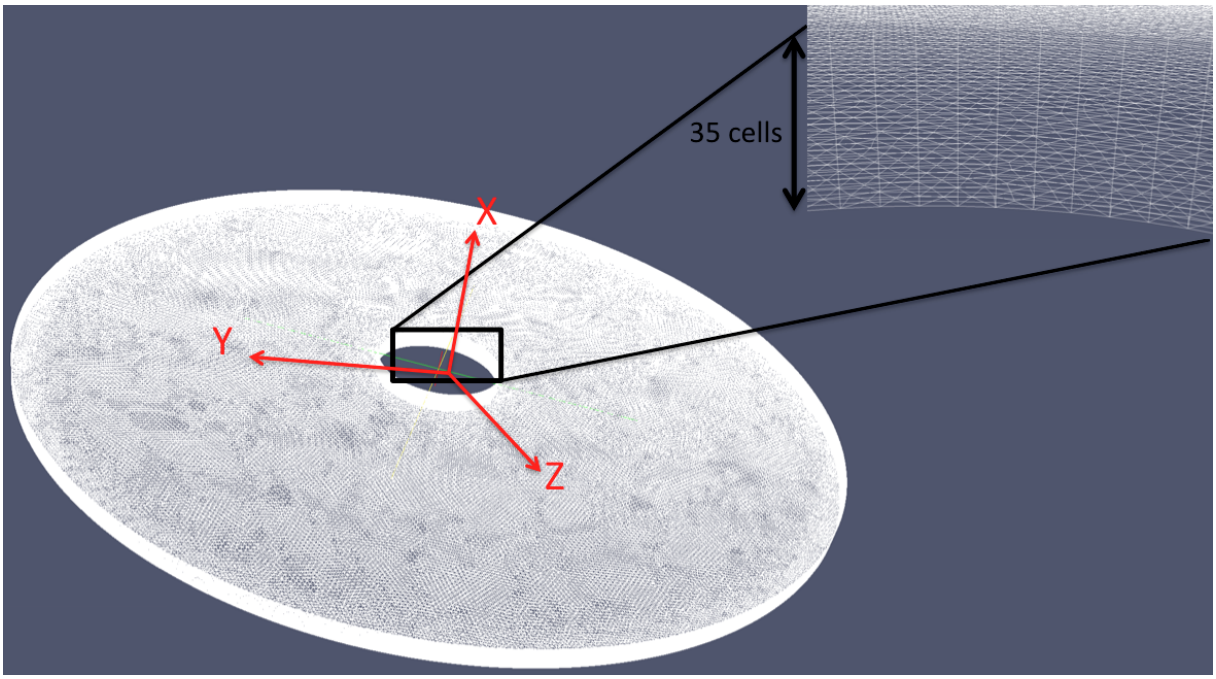

Figure 4.2: Smart mesh

In the third mesh, only a 120° section of the rotor-stator geometry was simulated as previous results successfully proved the system's axisymmetry, as expected. The resolution in the x-direction was increased to 50 cells. This mesh has a total of 967,000 nodes. It will be referred to as "camembert mesh". It is shown in figure 4.3.

In the camembert mesh, the two side cuts were assigned periodic rotating boundary condition. At first, the code would diverge because it could not handle the singularity at the intersection between the hub's rotating boundary condition with the side cut's periodic boundary condition. Therefore, at the intersection, the side cuts were assigned a fixed no slip boundary condition on from $r^* = 0$ to $r^* = 0.02$. The boundary patch had negligible effects on the rotating flow of the system.

For each mesh, simulations were run with the Lax-Wendroff numerical scheme coupled

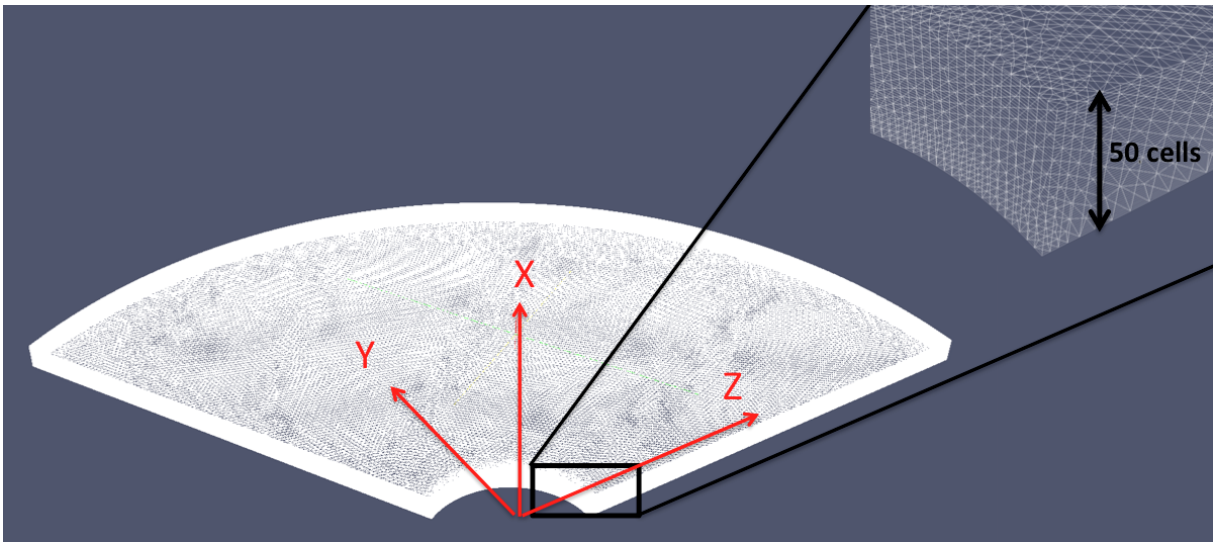

Figure 4.3: Camembert mesh

with both LES models Smagorinksy and WALE. However, only results with TTGC and Smagorinsky are shown because none of the simulations coupling TTGC and WALE converged.

4.2 Results

On each mesh, the results of simulations using combinations of the Lax-Wendroff and Two-step Taylor Galerkin schemes with the LES models Smaogrinksy and WALE are presented. Then, for each couple of numerical scheme and LES model, results depending on the meshes are shown.

4.2.1 First Mesh Results

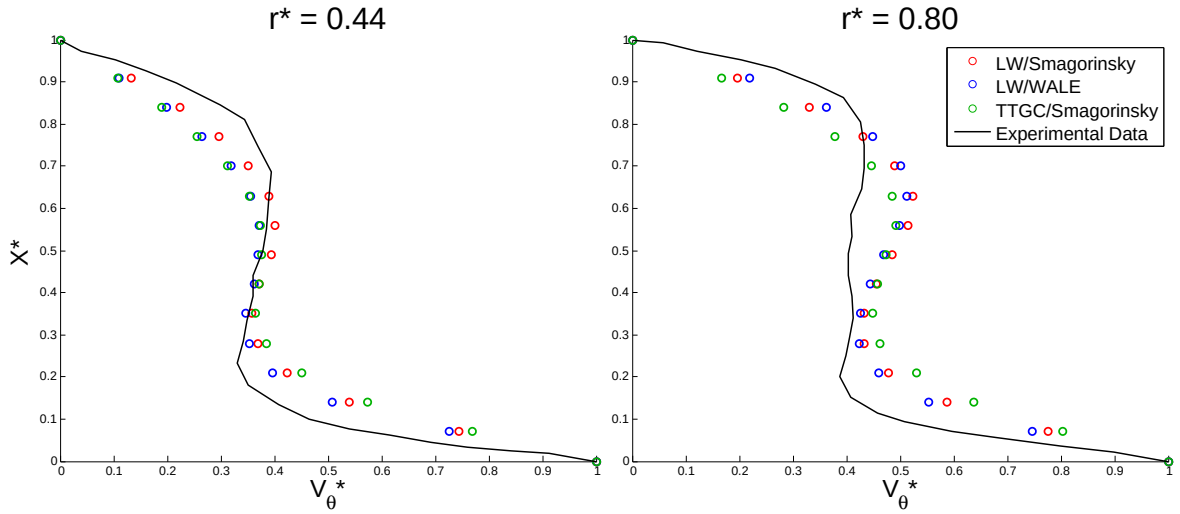

Figure 4.4: First mesh results for the tangential velocity V_θ

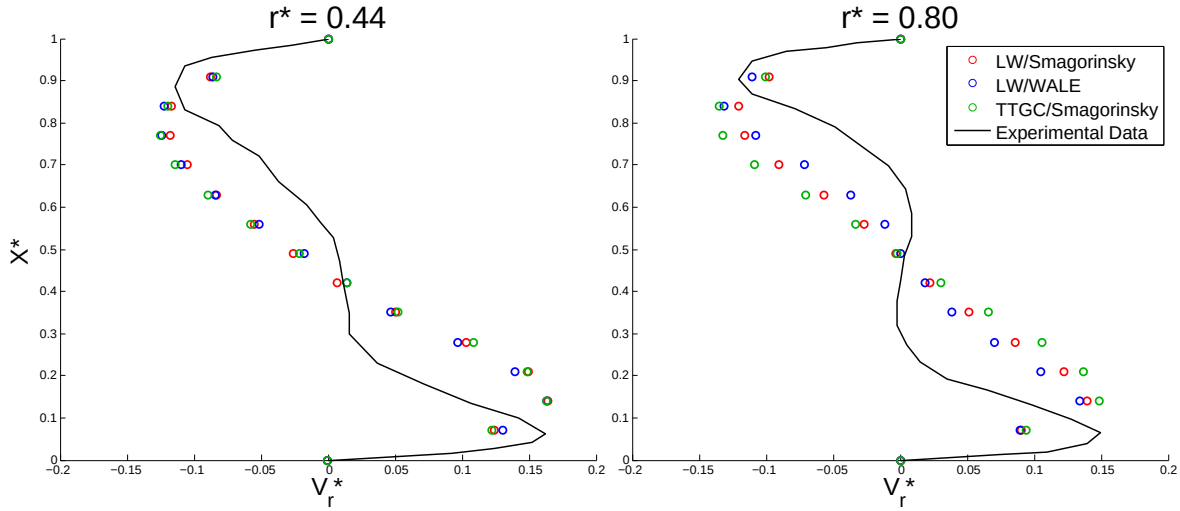

Figure 4.5: First mesh results for the radial velocity V_r

4.2.2 Smart Mesh Results

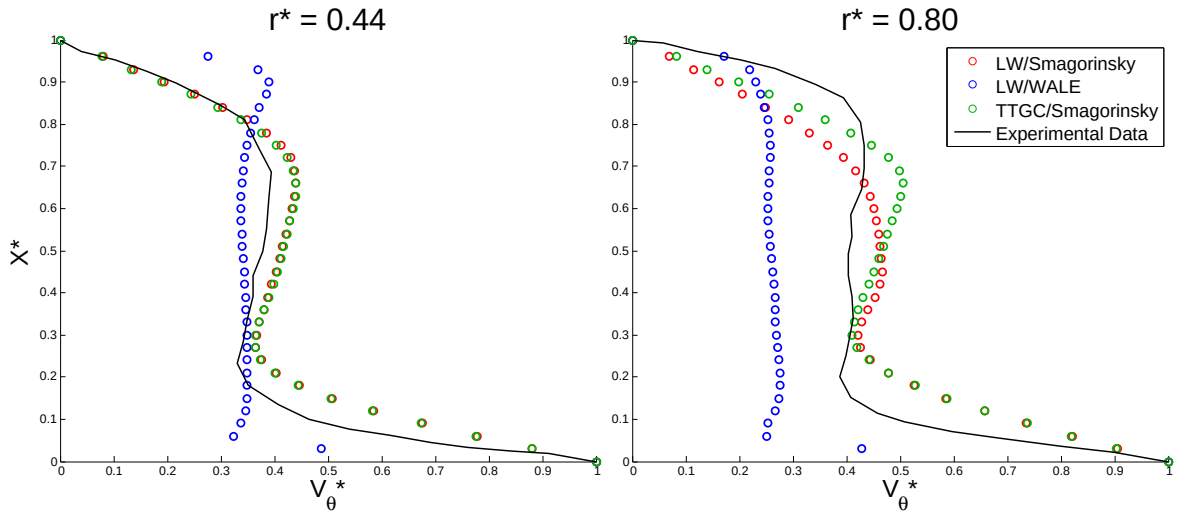

Figure 4.6: Smart mesh results for the tangential velocity V_θ

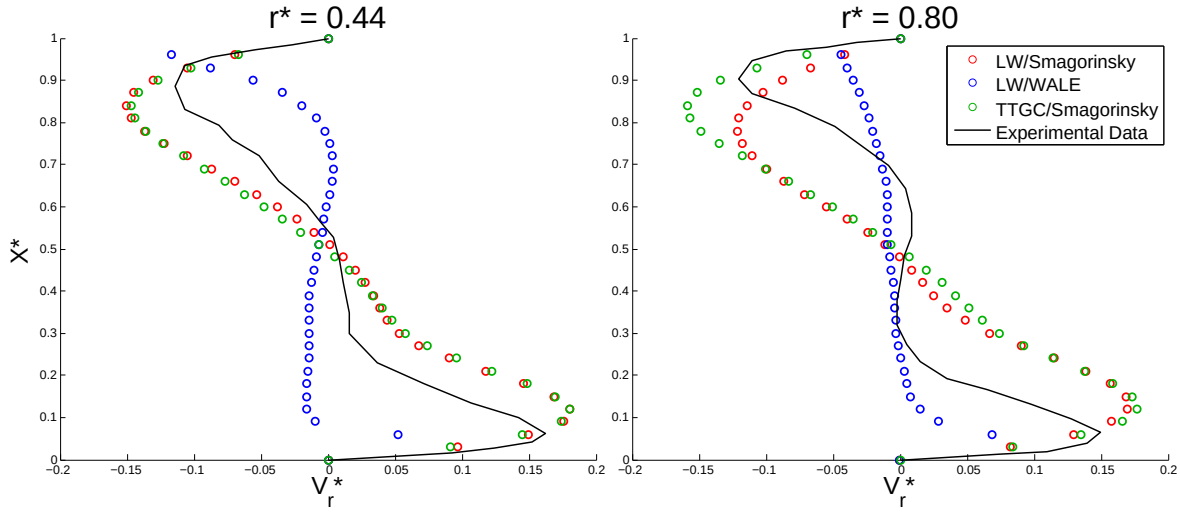

Figure 4.7: Smart mesh results for the radial velocity V_r

4.2.3 Camembert Mesh Results

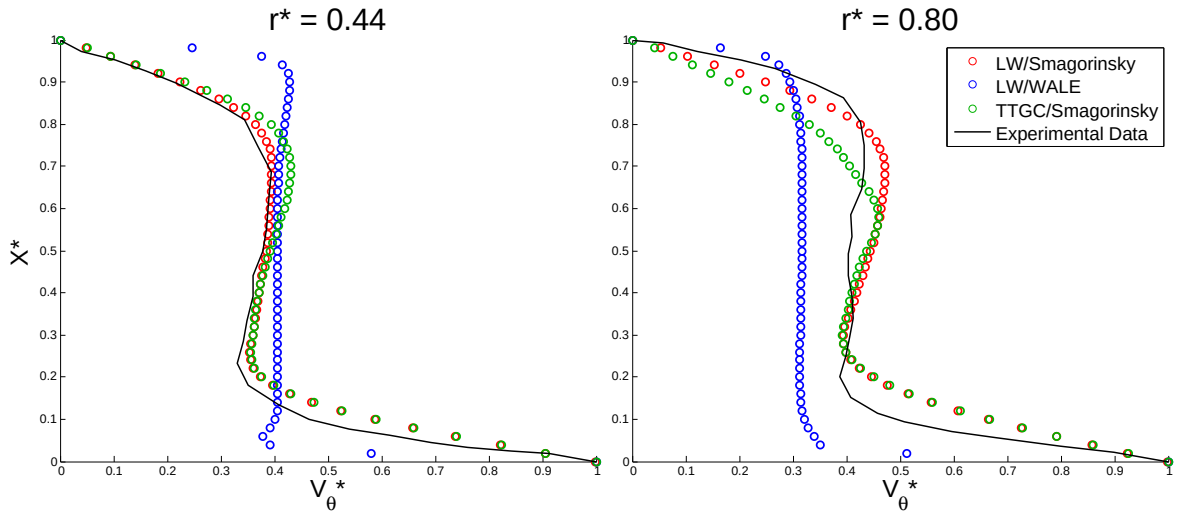

Figure 4.8: Camembert mesh results for the tangential velocity V_θ

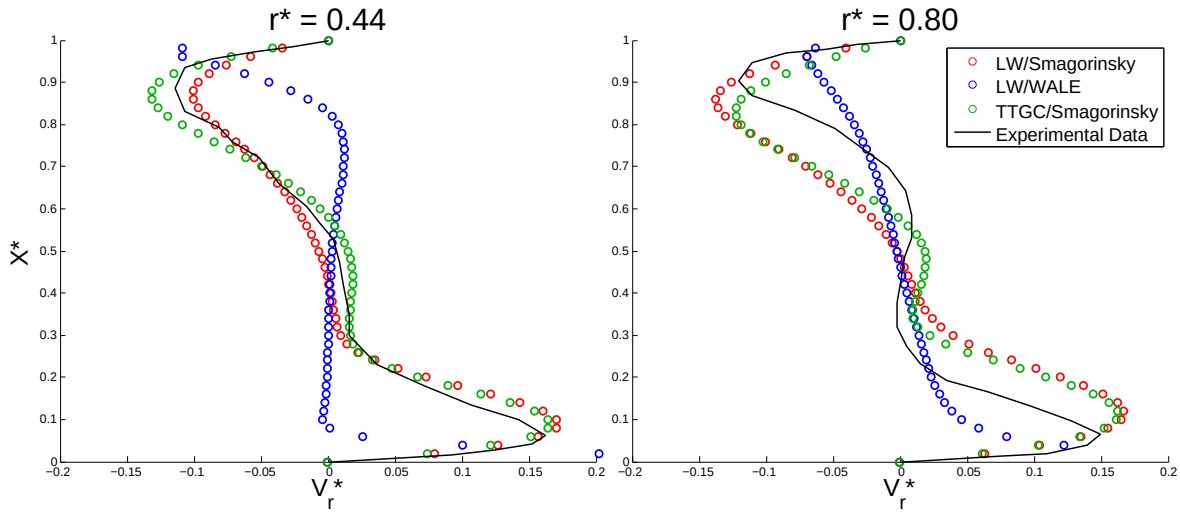

Figure 4.9: Camembert mesh results for the radial velocity V_r

4.2.4 Mesh Comparison Results

4.2.4.1 Lax-Wendroff with the Smagorinsky Model

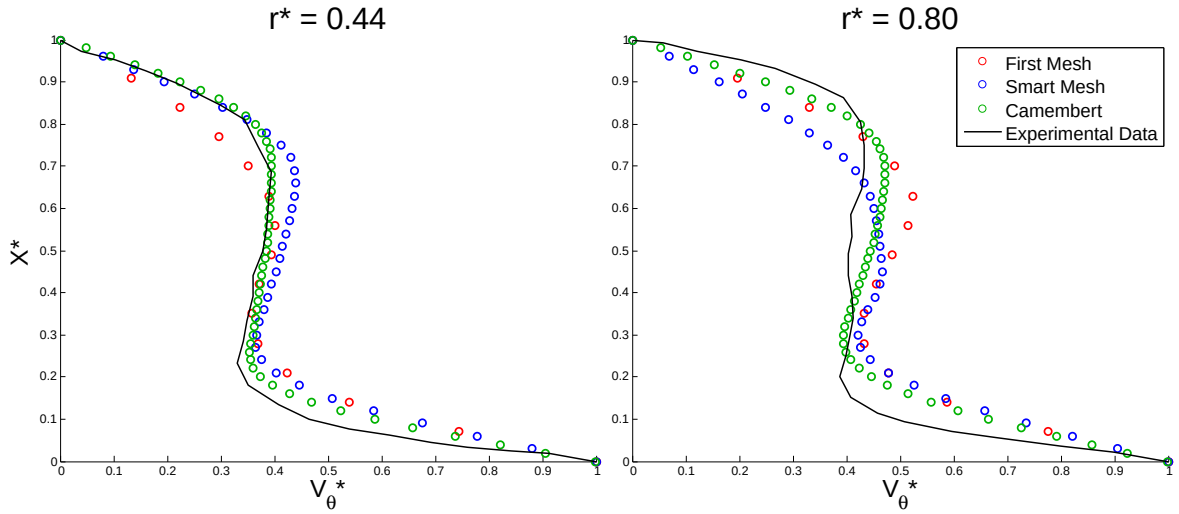

Figure 4.10: Mesh comparisons of the Lax-Wendroff scheme with the Smagorinsky model for the tangential velocity V_θ

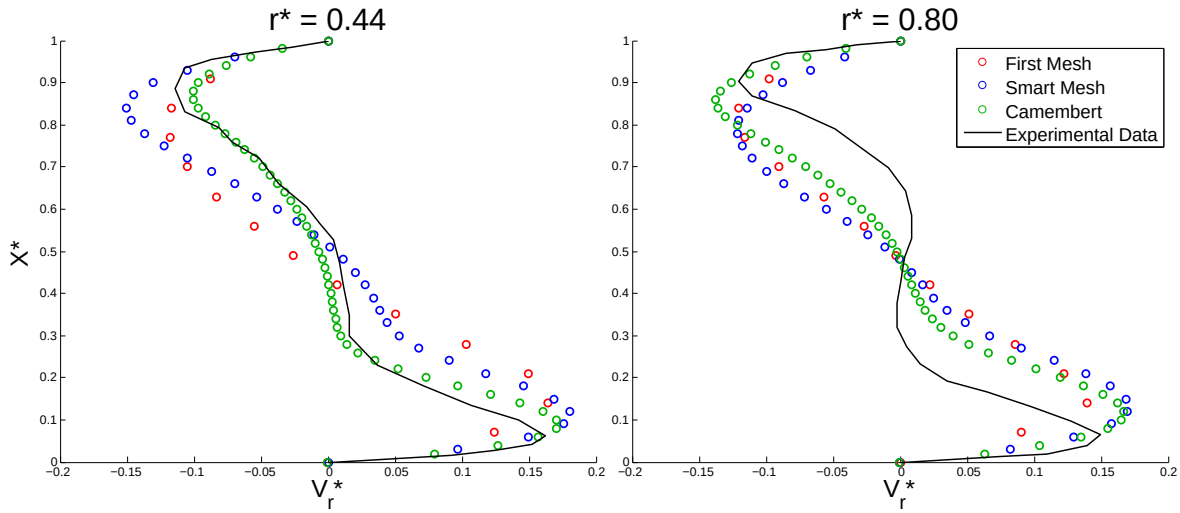

Figure 4.11: Mesh comparisons of the Lax-Wendroff scheme with the Smagorinsky model for the radial velocity V_r

4.2.4.2 Lax-Wendroff with the WALE Model

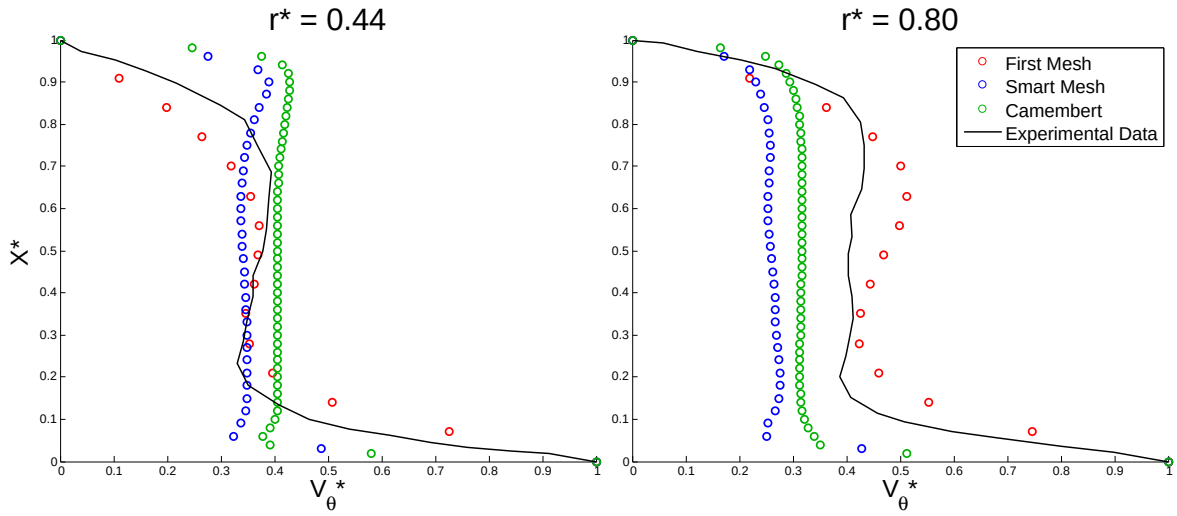

Figure 4.12: Mesh comparisons of the Lax-Wendroff scheme with the WALE model for the tangential velocity V_θ

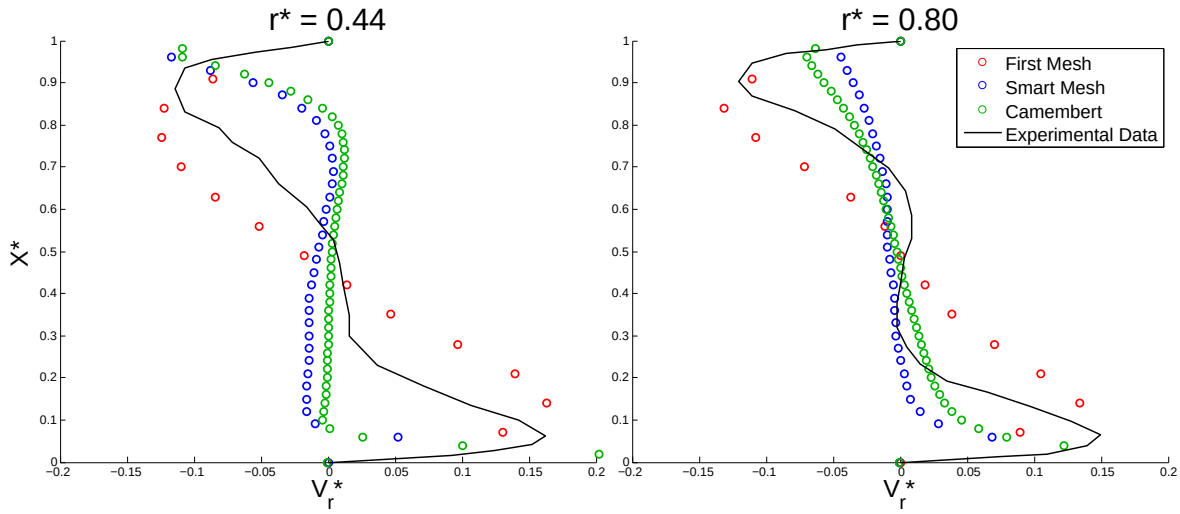

Figure 4.13: Mesh comparisons of the Lax-Wendroff scheme with the WALE model for the radial velocity V_r

4.2.4.3 Two-setp Taylor Galerkin with the Smagorinsky Model

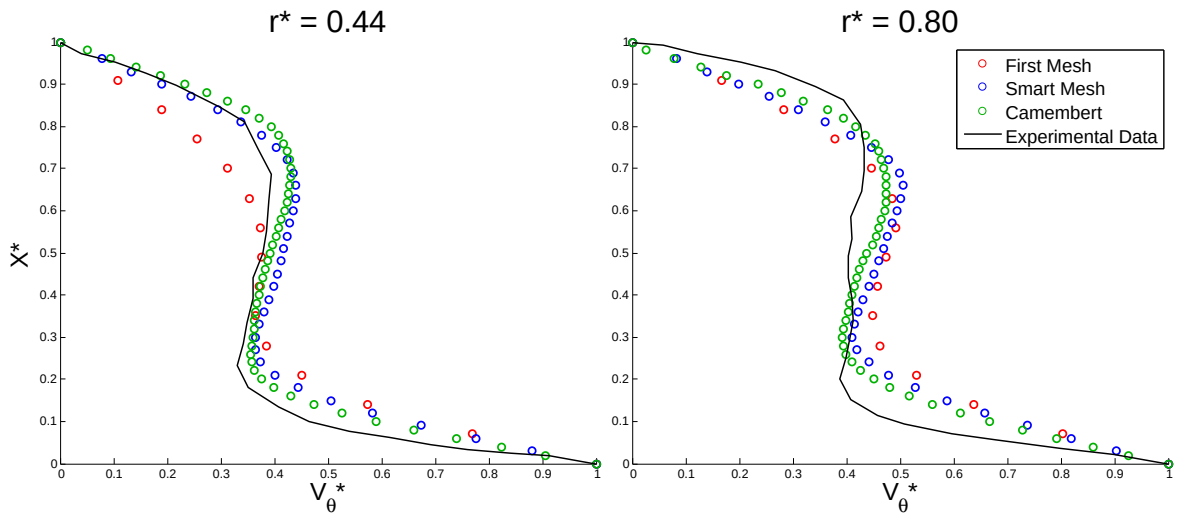

Figure 4.14: Mesh comparisons of the Lax-Wendroff scheme with the WALE model for the tangential velocity V_θ

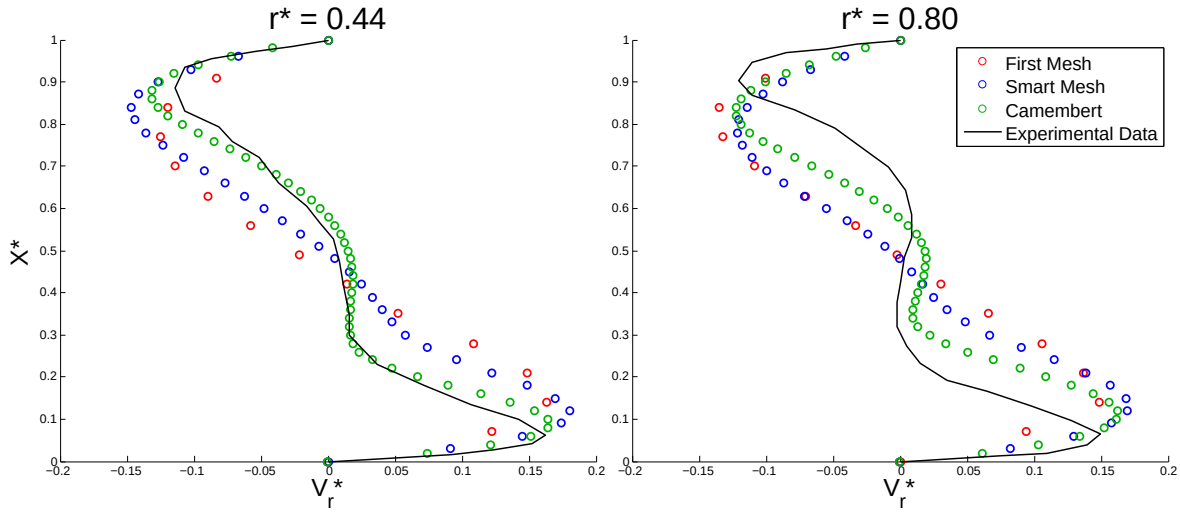

Figure 4.15: Mesh comparisons of the TTGC scheme with the Smagorinsky model for the radial velocity V_r

4.3 Discussion

On the first mesh, in figures 4.4 and 4.5, the simulations reproduce quantitatively the experimental results. The flow along the thickness can be divided in three distinct regions: a boundary layer on the rotor and the stator separated by a core region of approximately constant tangential velocity. For the three simulations, Lax-Wendroff with Smagorinsky, Lax-Wendroff with WALE, and TTGC with Smagorinsky, the overall shape of the velocity profiles were correctly obtained. From figure 4.4 and 4.5, the thickness of the two boundary layers seem to be overestimated by AVBP, especially at large radius. From figure 4.4 at $r^* = 0.44$, the the rotational velocity of the inner core is the same for the three simulations and the experimental results. However, at $r^* = 0.80$, the core velocity varies from 0.43 and 0.55 depending on the simulation. Also, from figure 4.5, in the three simulations, the core does not reach a region of zero radial velocity. These discrepancies may be explained by the lack of cells in each of the boundary layers. Only two or three mesh nodes are in the boundary layer obtained by the experimental results, which is greatly insufficient.

On the smart mesh, in figures 4.6 and 4.7 the two Smagorinsky simulations qualitatively reproduces the experimental results while the Lax-Wendroff with WALE simulation does not accurately obtain the desired velocity profiles. From figure 4.6, the WALE simulation underestimate the thickness of the rotor and stator boundary layer by a factor of 4 and the tangential velocity of the core by 40%. Comparing the two other simulations, for the tangential velocity in figure 4.6, the TTGC simulation seems closer to the experimental data than the Lax-Wendroff with Smagorinsky simulation, especially for $r^* = 0.80$. As for the first mesh, the rotational velocity of the core varies more with increasing radii. Also, the thickness of the boundary layers seem to be overestimated. In figures 4.7, for the radial velocity, the Lax-Wendroff with Smagorinsky and TTGC simulations obtained relatively similar results, except at $r^* = 0.80$ where the TTGC simulations seems to overestimate the the maxima velocity in the stator boundary layer by more than 50%.

On the camembert mesh, in figures 4.8 and 4.9, as for the smart mesh, the WALE

results do not capture correctly the velocity profiles obtained by the experimental data. The thickness of the boundary layer is greatly overestimated and the rotational velocity of the core is underestimated. Looking at the two other simulations, the Lax-Wendroff with Smagorinsky seems to be in better concordance with the experimental data than the TTGC simulation, especially for the tangential velocity at $r^* = 0.80$ on the stator side. This is surprising considering the TTGC is a higher order scheme than Lax-Wendroff. From 4.8 and 4.9, the two simulations seem to reproduce better the simulation at smaller radius. The rotor boundary layer and the tangential velocity of the core are correctly captured at $r^* = 0.44$ while, at $r^* = 0.80$, the former is overestimated by 70% and the latter is overestimated by up to 20%. In 4.9, the two simulations capture the region of zero radial velocity in the core, especially for $r^* = 0.44$. At $r^* = 0.80$, the velocity profiles are correctly reproduced but seem to be stretched towards the core region.

From the results of the three simulations ran in different meshes, it can first be concluded that the WALE LES model is not appropriate for the rotor-stator geometry. It clearly underestimates the thickness of both boundary layer and the velocity and the core. Also, although the TTGC scheme is about 2.5 times more expensive than the Lax-Wendroff scheme, it did not output substantially more accurate results despite being of higher order. Therefore, the Lax-Wendroff scheme coupled with the Smagorinsky LES model seems to be the best suited approach so numerically simulate the rotor-stator geometry.

In figures 4.10 through 4.15, the results of the three simulations Lax-Wendroff with Smagorinsky, Lax-Wendroff with WALE and TTGC with Smagorinsky are compared on the three meshes used. The Lax-Wendroff with WALE simulation, in figures 4.12 and 4.13, clearly differs from its two counterpart as the results' accuracy does not increase with the grid resolution in the thickness. The first mesh results qualitatively reproduce the experimental data. The three distinct regions, the rotor and stator boundary layer and the core, are clearly visible. However, in the smart mesh and camembert mesh results, the core region makes up for about 90% of the flow. The WALE model is clearly not appropriate to simulating the

rotor-stator system, especially if high grid resolution is desired along the thickness of the geometry. This may be due to the fact that the WALE model has a very low associated turbulent viscosity. By comparison, the turbulent viscosity is about 100 times stronger in the Smagorinsky model than in the WALE model. The strong viscosity helps capture the strong velocity gradients if the mesh is not fine enough. This also explains why the simulations with both TTGC and the WALE model did not converge. The Lax-Wendroff numerical scheme is of low-order and generates much more dissipation than the 3^{rd} order TTGC scheme. The relatively low viscosity and dissipation in the TTGC/WALE simulations lead to singularities next to the disks which in turn make the code diverge.

In figures 4.10 and 4.11, the results' accuracy are increasing with the grid resolution as expected. This is true especially for for smaller radius at $r^* = 0.44$. This can be explained by the fact that the larger the radius, the larger the local Reynolds number $\mathrm{Re}_r = \dfrac{\Omega r^2}{\nu}$. The increase in Re_r in turn increases the local turbulence. Therefore, if the accuracy of the simulation decreases with the radius, it implies that the grid resolution is not fine enough. This hypothesis is supported by figures 4.16 shown below.

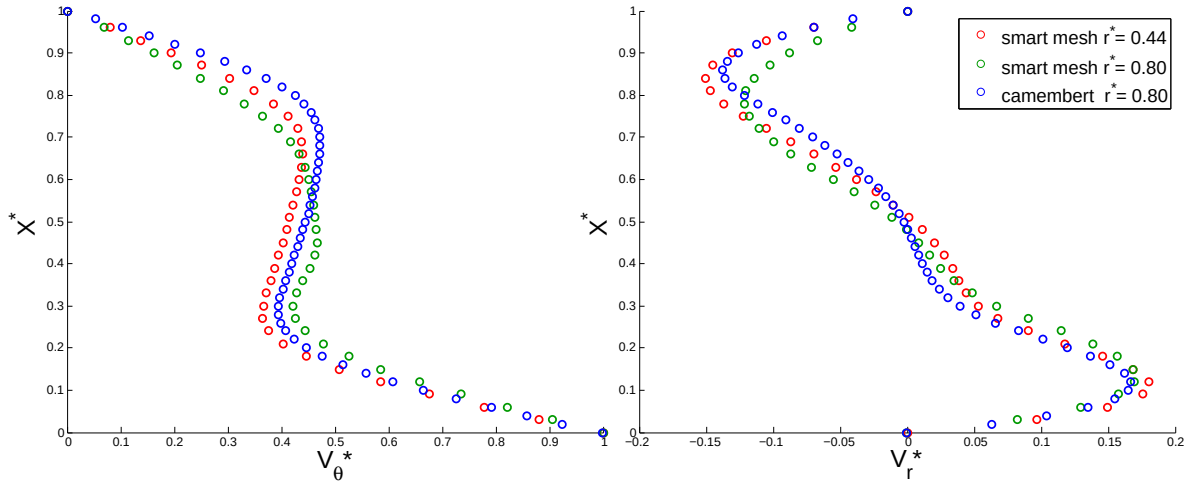

Figure 4.16: Comparisons of the camembert results at $r^* = 0.80$ with that of the smart mesh at $r^* = 0.44$ and $r^* = 0.80$ for the Lax-Wendroff Smagorinsky simulation.

Figure 4.16 shows that the results of the camembert mesh at $r^* = 0.80$ are similar to

that of the smart mesh at $r^* = 0.44$ than that at $r^* = 0.80$. As the smart mesh simulation at $r^* = 0.44$ where improved with the grid refinement along the thickness in the camembert mesh, the same can apply for the camembert mesh results at $r^* = 0.80$. It can therefore be concluded than although the camembert results at small radius are very satisfactory, the grid resolution along the thickness should be increased to obtain similar results at large radius.

In figures 4.14 and 4.15, as in the Lax-Wendroff with Smagorinsky simulations, the results's accuracy increases with the resolution of the grid, except in figure 4.14 at $r^* = 0.80$ where the velocity profile of the camembert mesh does not seem to capture well the boundary layer on the stator. In figure 4.15, only the camembert mesh is fine enough to capture the region of zero radial velocity in the core located between the two boundary layers. However, as for the smart mesh, the simulations for the camembert mesh at $r^* = 0.44$ for both velocity profiles are closer to the experimental data than the results at $r^* = 0.80$. Therefore, as for the smart mesh, it can be concluded that better results could be obtained with a finer grid along the thickness of the rotor-stator system.

CHAPTER 5

Conclusion

A large eddy simulation of an enclosed rotor-stator cavity of large aspect ratio, $G = 18.32$, has been performed. The rotational Reynolds number under consideration in this investigation was fixed to $Re = 9.5\text{x}10^4$. According to Poncet's work [20], [14], this configuration should correspond to a weakly turbulent flow, with turbulence intensities found only along the stator.

The simulations were performed on three different grids with different cell resolution along the thickness. The numerical schemes used are the second order Lax-Wendroff and third order Two-step Taylor Galerckin schemes. Two different LES models were tested, the classic Smagorinsky model and the WALE model. The mean velocity results were recored once the kinetic energy of the system converged. The results from the three grids yielded qualitatively satisfactory results. The Batchelor type of flow was correctly reproduced: a boundary layer on each disk separated by a core region of zero radial velocity and constant tangential velocity.

The WALE simulation results were on par with that of the Smagorinsky for the first mesh-the 14 axial cell resolution grid. However, for the two other grids of higher resolution in the thickness, it failed to reproduce correctly the mean velocity profiles. The boundary layer thickness along the two disk were underestimated by a factor of 5 while the core region velocity was underestimated by 44%. Also, it is important to note that no simulation were performed with both the TTGC scheme and the WALE model since no convergence could be achieved. This may be explained by the relatively low turbulent viscosity generated by the WALE model in comparison the Smagorinsky model. The turbulent viscosity helps capture

the strong velocity gradients in the boundary layers close to the disks.

The Smagorinsky simulation yielded very satisfactory results. As expected, the results discrepancy with the experimental results increased with the cell resolution along the thickness. Overall, a slight advantage to the TTGC scheme over the LW scheme was found although it was not always the case. Also, it was showed that better results could be obtained with an even higher resolution along the thickness direction.

References

[1] *T. Von Kármán, Uber laminar und turbulente Reibung, ZAMM 1 (4) ,1921.*

[2] *V.W. Ekman. On the influence of the Earths rotation on ocean-currents. Arkiv. Mat Astr. Fys., 2(11):152, 1905.*

[3] *U.T. Bödewadt. Die Drehströmung über festem Grunde. Z. Angew. Math. Mech., 20:241253, 1940.*

[4] *G.K. Batchelor. Note on a class of solutions of the Navier-Stokes equations representing steady rotationally-symmetric flow. Quat. J. Mech. and Appl. Math., 4(1):2941, 1951.*

[5] *K. Stewartson. On the flow between two rotating coaxial disks. Proc. Camb. Phil. Soc., 49:333341, 1953.*

[6] *H.O. Kreiss and S.V. Parter. On the swirling flow between rotating coaxial disks: existence and uniqueness. Commun. Pure Appl.Math., 36:5584, 1983.*

[7] *J. W. Daily, R. E. Nece. Chamber dimension effects on induced flow and frictional resistance of enclosed rotating disks. ASME J. Basic Eng., 82:217232, 1960.*

[8] *G.N. Lance and M.H. Rogers. The axially symetric flow of a viscous fluid between two infinite rotating disks. Proc. R. Soc. London A, 266:109121, 1962.*

[9] *J.M. Owen and R.H. Rogers. Flow and Heat Transfer in Rotating-Disc Systems - Vol.1: Rotor-Stator Systems. Ed. Morris, W.D. John Wiley and Sons Inc., New-York, 1989.*

[10] *Poncet S., Serre E., Large Eddy Simulation of Non-Isothermal Turbulent Rotor-Stator Flows, The Twelfth International Symposium on Transport Phenomena and Dynamics of Rotating Machinery (ISROMAC-12), Honolulu, 2008.*

[11] *Launder B.E., Tselepidakis D.P., Application of a new second-moment closure to turbulent channel flow rotating in orthogonal mode. Int. J. Heat Fluid Flow 15 (1), 2-10, 1994*

[12] *Elena L., Schiestel R., Turbulence modelling of rotating confined flows, Int. J. Heat Fluid Flow 17, 283-289, 1996*

[13] *Poncet S., Chauve M.P., Schiestel R., Batchelor versus Stewartson flow structures in a rotor- stator cavity with throughflow, Phys. Fluids 17, 075110, 2005*

[14] *Séverac E., Poncet S., Serre E., Chauve M.-P., Large eddy simulation and measurements of turbulent enclosed rotor-stator flows, Phys. Fluids, 19, 085113, 2007.*

[15] *E. Séverac and E. Serre. A spectral vanishing viscosity LES model for the simulation of turbulent flows within rotating cavities. submitted to J. Comp. Phys., 2006.*

[16] *Poncet S., Serre E., High-order LES of turbulent heat transfer in a rotor-stator cavity, Int. J. Heat Fluid Flow, 30 (4), p.590-601, 2009.*

[17] *Viazzo S., Poncet S., Serre E., Randriamampianina A., Bontoux P., High-order LES of confined rotor-stator flows, Flow, Turbulence and Combustion, 88 (1-2), p.63-75, 2012.*

[18] *E. Tadmor. Convergence of spectral methods for nonlinear conservation laws. SIAM J. Numer. Anal., 26(1):3044, 1989.*

[19] *Abide, S., Viazzo, S.: A 2D compact fourth-order projection decomposition method, J. Comp. Phys. 206, 252-276, 2005*

[20] *Poncet S., Randriamampianina A., Ecoulement turbulent dans une cavit rotor-stator ferme de grand rapport d'aspect, C.R. Mcanique, 333 (10), p.783-788, 2005.*

[21] *Randriamampianina A., Poncet S., Turbulence characteristics of the Bodewadt layer in a large enclosed rotor-stator system, Phys. Fluids, 18, 055104, 2006.*

[22] *Poncet S., Randriamampianina A., Three-dimensional turbulent boundary layer in a shrouded rotating system, Flow, Turbulence and Combustion, 80 (1), p.107-117, 2008.*

[23] *Poncet S., Chauve M.-P., Le Gal P., Turbulent Rotating Disk Flow with Inward Throughflow, J. Fluid Mech., 522, p.253-262, 2005.*

[24] *M. Lygren and H. I. Andersson. Turbulent flow between a rotating and a stationary disk. J. Fluid. Mech., 426:297326, 2001.*

[25] *Poinsot, Thierry, and Denis Veynante. Theoretical and Numerical Combustion. 3rd ed. Philadelphia: Edwards, 2005. Print.*

[26] *Smagorinksy, J., General circulation experiments with the primitive equations, I. the basic experiment. Monthly Weather Review 91, 3, 99-164, 1963*

[27] *Ducros, F., Nicoud, F., AND Poinsot, T. , Wall-adapting local eddy-viscosity models for simulations in complex geometries. In ICFD, B. M. J., Ed., pp. 293-300, 1998*

[28] *L. Gicquel, AVBP Handbook, AVBP_V6.0, 2008,*

http://www.cerfacs.fr/ avbp/AVBP_V6.X/HANDBOOK/AVBP/HTML2/main.html